

Charge versus energy transfer in atomically-thin graphene-transition metal dichalcogenide van der Waals heterostructures

Guillaume Froehlicher,* Etienne Lorchat, and Stéphane Berciaud†

Université de Strasbourg, CNRS, Institut de Physique et Chimie des Matériaux de Strasbourg (IPCMS), UMR 7504, F-67000 Strasbourg, France

Van der Waals heterostructures, made from stacks of two-dimensional materials are promising for novel optoelectronic devices. The performance of such devices is governed by near-field coupling through, e.g., interlayer charge and/or energy transfer. New concepts and experimental methodologies are needed to properly describe atomically thin heterointerfaces. Here, we report an original study of interlayer charge and energy transfer in single-layer graphene/single-layer molybdenum diselenide (MoSe_2) heterostructures using a combination of micro-photoluminescence and Raman scattering spectroscopies. The photoluminescence intensity in Gr/MoSe_2 is massively quenched and rises linearly with the photon flux, demonstrating a drastically shortened (~ 1 ps) room temperature exciton lifetime in MoSe_2 . Key complementary insights are provided from a comprehensive analysis of the graphene and MoSe_2 Raman modes, which reveals a net photoinduced electron transfer from MoSe_2 to graphene and hole accumulation in MoSe_2 . Remarkably, as the photon flux increases, the steady state Fermi energy of graphene saturates at 290 ± 15 meV above the Dirac point. This reproducible behavior is observed both in ambient air and in vacuum and is discussed in terms of intrinsic factors (i.e., band offsets) and environmental effects. In this regime, balanced photoinduced flows of electrons and holes transfer to graphene, a mechanism that can be assimilated to an energy transfer process. The absence of correlation between exciton dynamics and the presence of a net charge transfer strongly suggests that non-radiative interlayer energy transfer, either in the form of exciton transfer or balanced electron and hole transfer is the dominant coupling mechanism between atomically-thin transition metal dichalcogenides and graphene.

I. INTRODUCTION

Charge and energy transfer (CT, ET) play a prominent role in atomic, molecular and nanoscale systems. On the one hand, Förster-type energy transfer [1], mediated by relatively long-range (up several nm) near-field dipole-dipole coupling is an essential step in photosynthesis [2] and is now engineered in a variety of light-harvesting devices and distance sensors [3, 4]. Charge transfer, on the other hand is a much shorter range process (~ 1 nm) that plays a key role in a number of molecular and solid-state systems and is at the very origin of the operation of photodetectors and solar cells [5, 6]. In the limit of orbital overlap between donor and acceptor systems, electron exchange, resulting in no net charge transfer and also known as Dexter-type energy transfer [7], may also occur. The efficiencies of CT and ET depend very sensitively on the donor-acceptor distance, on the energy levels (or bands) offsets, and on the local dielectric and electrostatic environment. CT and ET processes may have beneficial or detrimental impact on the performance of optoelectronic devices and therefore deserve dedicated, fundamental investigations.

In this context two-dimensional materials (2DM, such as graphene, boron nitride, transition metal dichalcogenides (TMDs), black phosphorus,...) provide an extraordinary toolkit to investigate novel regimes of

CT/ET. Indeed the very diverse and complementary physical properties of 2DM can be tailored and controlled at the single-layer level, but also combined and possibly enhanced within so-called van der Waals heterostructures (vdWHs) [8–10]. VdWHs provide a new paradigm of clean, ultra smooth 2D heterointerfaces [11]. Since their van der Waals gap is only of a few Å, band bending and depletion regions cannot develop in vdWH. As a result, well-established concepts borrowed from the physics of bulk or low-dimensional heterojunctions [6] must be adapted with great care when describing the optoelectronic response of vdWHs. In addition, the ultimate proximity between the atomically thin building blocks that compose a vdWH potentially allows ultra efficient CT and/or ET.

Among the vast library of 2DM, graphene [12] and atomically-thin semiconducting TMDs (with formula MX_2 , with $\text{M} = \text{Mo, W}$ and $\text{X} = \text{S, Se, Te}$) [10, 13, 14] have attracted particular interest for the development of novel optoelectronic devices [15–25]. Indeed, graphene (Gr) may act as a highly tunable transparent electrode, endowed with exceptional physical properties [26–28], while monolayer TMDs are direct bandgap semiconductors with unusually strong light-matter interactions and excitonic effects [10, 29, 30], as well as unique spin, valley and optoelectronic properties [10, 30, 31]. Photodetectors based on graphene and TMDs display high photoresponsivity and photogain [15–19], down to picosecond timescales [20]. The photophysics of Gr/TMD vdWHs is governed by near-field interlayer CT and/or ET (ICT, IET). In the related and most studied case of TMD/TMD heterojunctions with type II band align-

* Present address: Department of Physics, University of Basel, Klingelbergstrasse 82, CH-4056 Basel, Switzerland.

† stephane.berciaud@ipcms.unistra.fr

ment, sub-picosecond ICT and subsequent interlayer exciton formation is thought to be the dominant coupling mechanism [31–36]. However, recent photoluminescence excitation spectroscopy studies in $\text{MoSe}_2/\text{WS}_2$ vdWH have suggested that IET may be at least as efficient as ICT [37].

In contrast, fundamental studies of IET and ICT remain scarce in Gr/TMD vdWH. Photoinduced ICT has been observed in Gr/MoS_2 photodetectors [18]. Recent transient absorption studies have evidenced fast interlayer coupling in Gr/WS_2 vdWHs and tentatively assigned it to photoinduced ICT [24]. Yet, such studies were mostly performed under ambient conditions and the share of environmental effects needs to be assessed. In addition, these works overlooked IET as a competing exciton decay pathway, even though related studies in hybrid heterostructures composed of nanoscale emitters (molecules, quantum dots, quantum wells,...) interfaced with carbon nanotubes [38], graphene [39–42], TMD [43, 44] have consistently demonstrated highly efficient Förster-type ET.

Unraveling the relative efficiencies of ICT and IET is of utmost importance for optoelectronics. For this purpose, optical spectroscopy offer minimally invasive and spatially-resolved tools. First exciton dynamics and interlayer coupling can be probed with great sensitivity using micro-photoluminescence (PL) spectroscopy [10, 31]. Second, micro-Raman scattering spectroscopy allows quantitative measurements of doping and charge transfer as it has been demonstrated in graphene [45–49] and in MoS_2 [50, 51], but not yet in vdWHs.

In this paper, we make use of PL and Raman spectroscopies to investigate interlayer coupling in model vdWHs made of single-layer graphene stacked onto single-layer molybdenum diselenide (MoSe_2) (hereafter denoted Gr/MoSe_2) *in the absence of any externally applied electric field*. While highly efficient exciton-exciton annihilation and subsequent saturation of the PL intensity is – as expected – observed in bare MoSe_2 as the incident photon flux increases, the PL in Gr/MoSe_2 is massively quenched and its intensity rises linearly with the photon flux, demonstrating a drastically shortened room-temperature exciton lifetime in MoSe_2 . Key complementary insights are provided from a comprehensive analysis of the graphene and MoSe_2 Raman modes, which reveals a net photoinduced electron transfer from MoSe_2 to graphene and hole accumulation in MoSe_2 . Remarkably, as the photon flux increases, the steady state Fermi energy of graphene saturates at 290 ± 15 meV above the Dirac point. In this regime, balanced flows of electrons and holes transfer to graphene, resulting in no net photoinduced charge transfer. This reproducible behavior is observed both in ambient air and in vacuum and is discussed in terms of intrinsic factors (i.e., band offsets) and extrinsic effects associated with native doping and charge trapping. The absence of correlation between exciton dynamics and the presence of a net charge transfer strongly suggests that non-radiative interlayer

energy transfer, either in the form of exciton transfer or balanced electron and hole transfer is the dominant coupling mechanism between atomically-thin transition metal dichalcogenides and graphene. Our results provide a better understanding of the atomically thin two-dimensional metal-semiconductor (i.e., Schottky) junction, an ubiquitous building block in emerging optoelectronic devices, and will serve as a guide to engineer charge carrier and exciton transport in two-dimensional materials.

II. CHARACTERIZATION OF THE Gr/MoSe_2 HETEROSTRUCTURE

Figure 1(a) shows an optical image of a Gr/MoSe_2 vdWH (Sample S₁) deposited onto a Si/SiO_2 substrate. From AFM measurements (see Supplemental Material [52], Fig. S1), we can distinguish a region of the heterostructure (highlighted with a white dashed contour in Fig. 1(a)), where the two layers are well coupled, as evidenced by the small surface roughness [9] and the small height difference of approximately 0.65 nm between the surface of MoSe_2 and Gr (see Fig. 1(b)). Outside this region, the interface shows sub-micrometer size “pockets” and an average step of $\sim 2 - 3$ nm (see Fig. 1(b)) between MoSe_2 and Gr . Hereafter, the former and the latter are referred to *coupled* and *decoupled* Gr/MoSe_2 , respectively (see Fig 1(c) and Supplemental Material [52], Fig. S1).

Typical photoluminescence (PL) and Raman spectra from three different points of the sample are shown in Fig. 1(d) and Fig. 1(e), respectively. Figure 1(f-k) displays the hyperspectral maps of (f) the MoSe_2 PL intensity, (g-j) the frequencies ($\omega_{\text{G},2\text{D}}$) and full-widths at half maximum (FWHM, $\Gamma_{\text{G},2\text{D}}$) of the Raman G- and 2D-mode features [53], and (k) of the ratio of their integrated intensities ($I_{2\text{D}}/I_{\text{G}}$). Note that no defect-induced D-mode feature [53] (expected around 1350 cm^{-1}) emerges from the background showing the very good quality of our sample. All hyperspectral maps allow to distinctively identify the coupled and decoupled Gr/MoSe_2 regions and confirm the trends observed on selected points.

The PL spectra in Fig. 1(d) are characteristic of single-layer MoSe_2 with the A and B excitons [54] near 1.57 eV and 1.75 eV, respectively. Remarkably, the MoSe_2 PL intensity is ~ 300 times smaller on coupled Gr/MoSe_2 than on $\text{MoSe}_2/\text{SiO}_2$, while it is only reduced by a modest factor of ~ 2 on decoupled Gr/MoSe_2 (Fig. 1(d,f)). Such massive PL quenching, also observed for other Gr/TMD vdWHs [20, 24] demonstrates strong interlayer coupling and suggest a much reduced exciton lifetime.

As shown in Fig. 1(e),(g-k), interlayer coupling also dramatically affects the Raman response of graphene. Indeed, on coupled Gr/MoSe_2 , the G-mode feature upshifts, gets narrower, and the $I_{2\text{D}}/I_{\text{G}}$ ratio decreases (Fig. 1(k)) with respect to reference measurements on the neighboring pristine graphene deposited

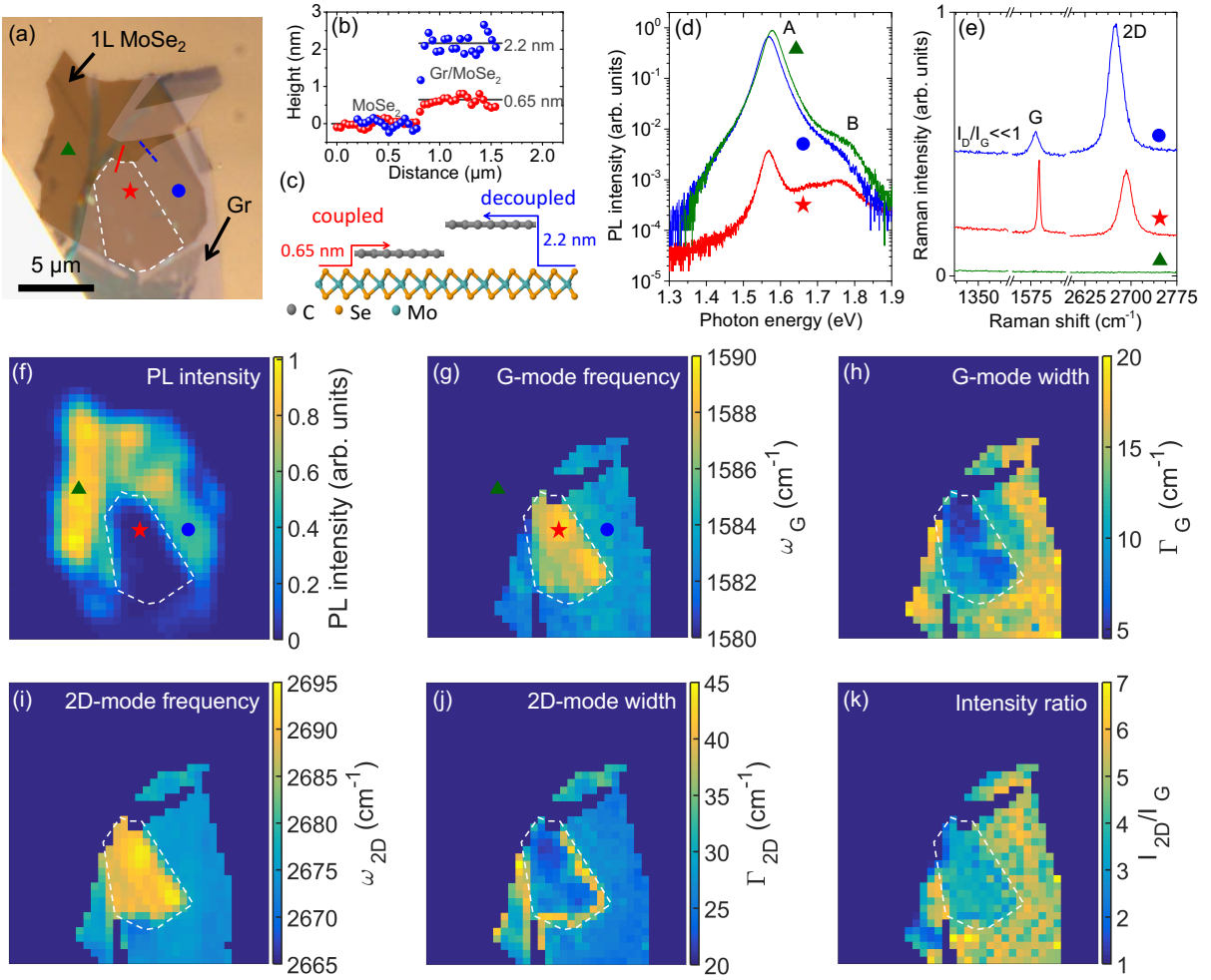


FIG. 1. (a) Optical image of a single-layer graphene/single-layer MoSe₂ van der Waals heterostructure deposited onto a Si/SiO₂ substrate (sample S₁). The coupled part of the heterostructure is represented by the white dashed contour. (b) Height profiles, measured by atomic force microscopy, along the dashed blue and red lines drawn in (a). (c) Schematic of the heterostructure showing the coupled and decoupled regions. Photoluminescence (d) and Raman scattering (e) spectra recorded on the three spots shown in (f) and (g), respectively. In (d) and (e), the spectra are plotted with the same color as the symbols in (f) and (g), respectively. (f) MoSe₂ photoluminescence intensity map. (g-k) Hyperspectral Raman maps of the (g) G-mode frequency ω_G , (h) G-mode FWHM Γ_G , (i) 2D-mode frequency ω_{2D} , (j) 2D-mode FWHM Γ_{2D} , and (k) ratio between the integrated intensities of the 2D- and G-mode features (I_{2D}/I_G) measured on single-layer graphene. All maps have the same scale as in (a) and were recorded in ambient air with an incident photon flux $\Phi_{ph} = 2 \times 10^{19} \text{ cm}^{-2} \text{ s}^{-1}$ and $\Phi_{ph} = 2 \times 10^{22} \text{ cm}^{-2} \text{ s}^{-1}$ for photoluminescence and Raman measurements, respectively.

on SiO₂ (Gr/SiO₂) and decoupled Gr/MoSe₂ regions (Fig. 1(e,k)). These observations are robust evidence of an increased charge carrier concentration in graphene [47, 48]. Surprisingly, we also observe an upshift of the 2D-mode frequency on coupled Gr/MoSe₂ (Fig. 1(i)), which is too high to be solely induced by doping or strain [48, 55, 56], and seems qualitatively similar to previous reports on graphene deposited on thick boron nitride terraces [57, 58] and monolayer MoS₂ grown on graphene [21]. Possible origins for this upshift are discussed in the Supplemental Material [52] (Fig. S15).

In the following we quantitatively investigate exciton dynamics (Sec. III) and interlayer charge transfer

(Sec. IV).

III. EXCITON DYNAMICS IN Gr/MoSe₂

Figure 2(a,b) displays the normalized PL spectra of MoSe₂ recorded on MoSe₂/SiO₂, decoupled and coupled Gr/MoSe₂ at low and high incident photon flux Φ_{ph} . The A exciton PL feature of coupled Gr/MoSe₂/SiO₂ is marginally redshifted (by ≈ 10 meV) with respect to that of air/MoSe₂/SiO₂, irrespective of Φ_{ph} . Considering the drastically different dielectric environments, such a surprisingly small reduction of the *optical* bandgap is

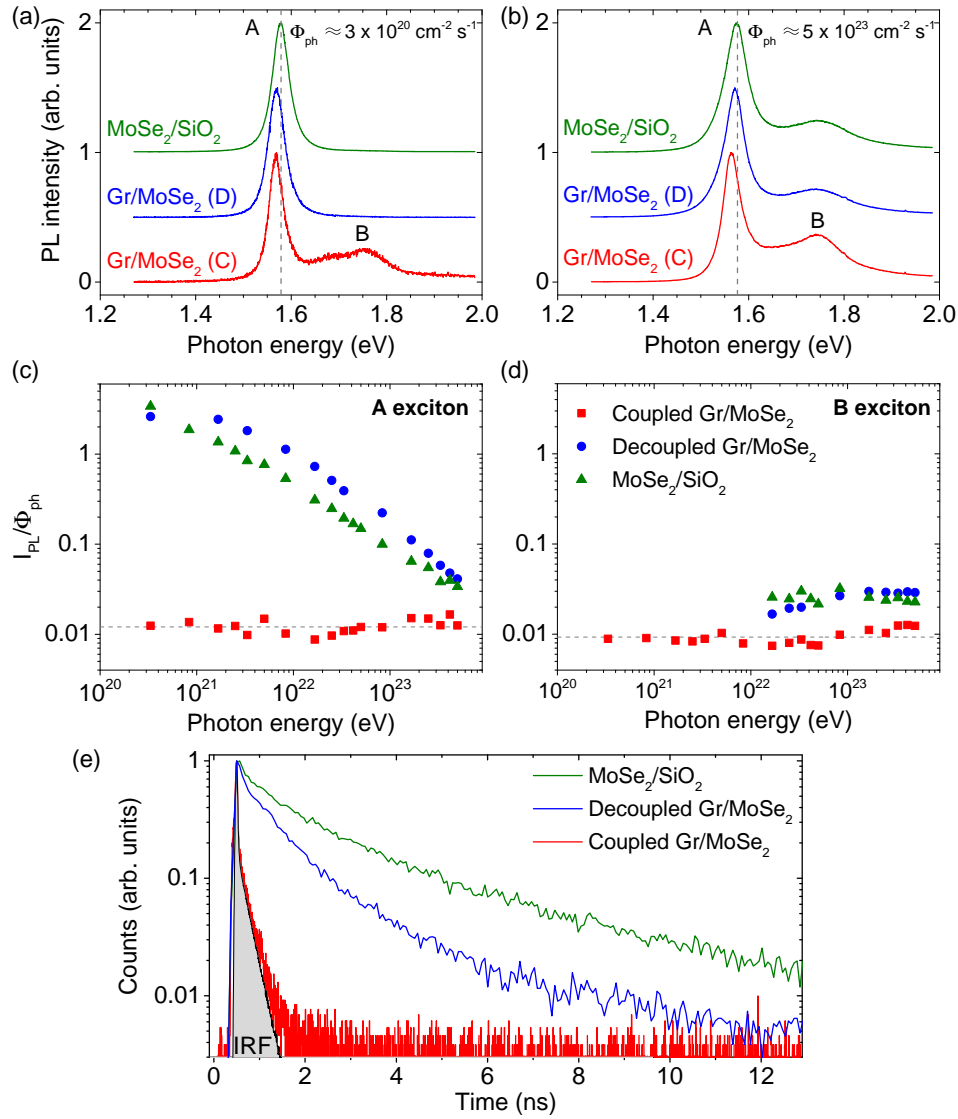


FIG. 2. Normalized photoluminescence spectra of MoSe₂ recorded at an incident photon flux (a) $\Phi_{ph} = 3 \times 10^{20} \text{ cm}^{-2} \text{ s}^{-1}$ and (b) $\Phi_{ph} = 5 \times 10^{23} \text{ cm}^{-2} \text{ s}^{-1}$ for MoSe₂/SiO₂, decoupled (D) and coupled (C) Gr/MoSe₂. The A and B excitons are labeled and the position of the A exciton in MoSe₂/SiO₂ is indicated by a gray vertical dashed line. (b) Integrated photoluminescence intensity of the (c) A and (d) B exciton normalized by Φ_{ph} as a function of Φ_{ph} . The gray dashed line is a guide to the eye. The error bars are smaller than symbol size. (e) Photoluminescence decays recorded using a pulsed laser at 1.96 eV with a fluence of $\approx 2.2 \times 10^{11} \text{ cm}^{-2}$ per pulse. The gray area corresponds to the instrument response function (IRF). All measurements were performed in ambient air.

assigned to the near-perfect compensation of the reductions of electronic bandgap and exciton binding energy in graphene-capped MoSe₂[59–61]. The lineshapes of the A exciton features are quite similar, except for a small but reproducible narrowing of the A-exciton linewidth in coupled Gr/MoSe₂. Similar narrowing has recently been observed in TMD layers fully encapsulated in boron nitride [62, 63] and likely results from a reduction of inhomogeneous broadening and pure dephasing in graphene-capped TMD samples.

The integrated PL intensities of the A and B exci-

ton features (denoted $I_{PL}^{A,B}$) normalized by Φ_{ph} , are plotted as a function of Φ_{ph} in Figure 2(c) and (d), respectively. For MoSe₂/SiO₂ and decoupled Gr/MoSe₂, I_{PL}^A/Φ_{ph} drops abruptly as Φ_{ph} augments due to highly efficient exciton-exciton annihilation (EEA), as previously evidenced in TMD monolayers [64, 65]. In the case of coupled Gr/MoSe₂, I_{PL}^A/Φ_{ph} remains constant, within experimental accuracy, up to $\Phi_{ph} \sim 10^{24} \text{ cm}^{-2} \text{ s}^{-1}$. As a result, while I_{PL}^A is about 300 times weaker on coupled Gr/MoSe₂ than on bare MoSe₂ at $\Phi_{ph} = 3 \times 10^{20} \text{ cm}^{-2} \text{ s}^{-1}$, this quenching factor reduces down to

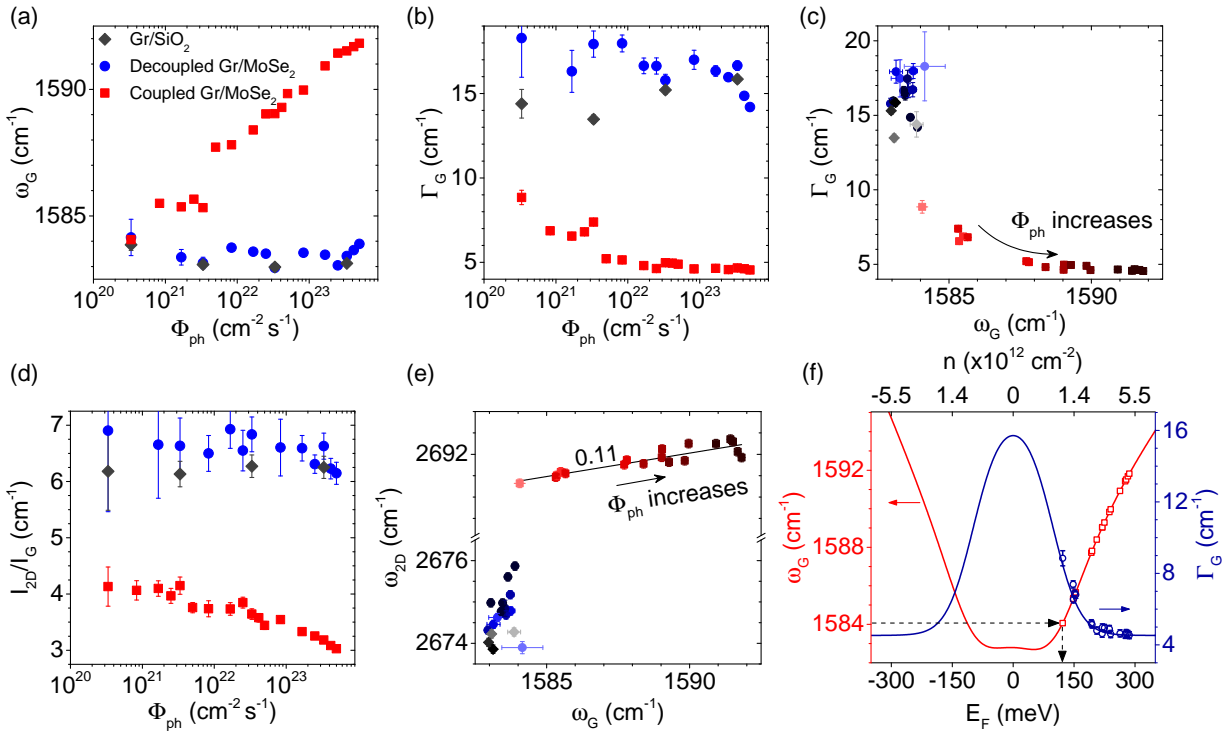


FIG. 3. (a) Raman G-mode frequency ω_G and (b) full-width at half maximum Γ_G recorded as a function of the incident photon flux Φ_{ph} for coupled (red squares) and decoupled (blue circles) Gr/MoSe₂ and for Gr/SiO₂ (gray diamonds) (see Figure 1). (c) Correlation between Γ_G and ω_G under increasing Φ_{ph} . (d) ratio between the integrated intensity of the 2D-mode feature and that of the G-mode feature I_{2D}/I_G as a function of Φ_{ph} . (e) Correlation between ω_{2D} and ω_G under increasing Φ_{ph} . The color of the symbols in (c) and (f) gets darker with increasing Φ_{ph} . (f) ω_G (red squares, left axis) and Γ_G (blue circles, right axis) as a function of the graphene Fermi energy E_F^{Gr} and doping level n_{Gr} . The solid lines are theoretical calculations [46, 48]. All measurements were performed in ambient air.

~ 3 at $\Phi_{ph} = 6 \times 10^{23} \text{ cm}^{-2} \text{ s}^{-1}$. Strong PL quenching together with the linear scaling of I_{PL}^A with Φ_{ph} demonstrate that interlayer coupling between graphene and MoSe₂ opens up non-radiative decay channel for A excitons, that dramatically reduces of the A exciton lifetime and is sufficiently fast to bypass EEA. The shortening of the A exciton lifetime is further substantiated by the analysis of the *hot* luminescence from the B exciton (note that our samples are photoexcited at 2.33 eV, i.e., well-above the B exciton in MoSe₂). In bare MoSe₂ and decoupled Gr/MoSe₂, $I_{PL}^A \gg I_{PL}^B$, whereas $I_{PL}^B \sim I_{PL}^A$ in coupled Gr/MoSe₂. Interestingly, I_{PL}^B is very similar in the three cases and scales linearly with Φ_{ph} (see Fig. 2(d)). These observations suggest (i) that interlayer coupling does not significantly affect exciton formation and exciton decay until a population of A excitons is formed, and (ii) that the A exciton lifetime in Gr/MoSe₂ is not appreciably longer than the B \rightarrow A decay time. The latter is typically in the subpicosecond range [66] in atomically thin TMDs, and provides a lower bound for the A exciton lifetime in Gr/MoSe₂. Additional insights are also given by time-resolved photoluminescence measurements recorded in ambient conditions (see Fig. 2(e)). Bare MoSe₂ and decoupled Gr/MoSe₂ dis-

play non-monooexponential decays [67] with average exciton lifetime of ~ 1 ns. As anticipated, the PL decay of Gr/MoSe₂ is too fast to be resolved using our experimental apparatus, confirming that the A exciton lifetime is significantly shorter than our time-resolution of ~ 20 ps. Using the estimated decay time of bare MoSe₂ and a typical quenching factor of ~ 300 in the low fluence limit, we can reckon a conservative upper bound of a few ps for the exciton lifetime in coupled Gr/MoSe₂.

IV. INTERLAYER CHARGE TRANSFER

A. Net photoinduced electron transfer to graphene

Fig. 3 shows the evolution of $\omega_{G,2D}$, $\Gamma_{G,2D}$ and I_{2D}/I_G measured in sample S₁ as a function of Φ_{ph} , in ambient air. The corresponding spectra are shown in the Supplemental Material [52] (Fig. S2). First, for Gr/SiO₂ and decoupled Gr/MoSe₂, $\omega_G \approx 1583 \text{ cm}^{-1}$, $\Gamma_G \approx 16 \text{ cm}^{-1}$, $\omega_{2D} \approx 2674 \text{ cm}^{-1}$ and $I_{2D}/I_G \approx 6.5$ do not show any appreciable variation as Φ_{ph} augments. These values correspond to very weakly doped graphene ($|n_{Gr}| \sim 10^{11} \text{ cm}^{-2}$ or $|E_F^{Gr}| \lesssim 100 \text{ meV}$) [47, 48, 68]. In addition, the ab-

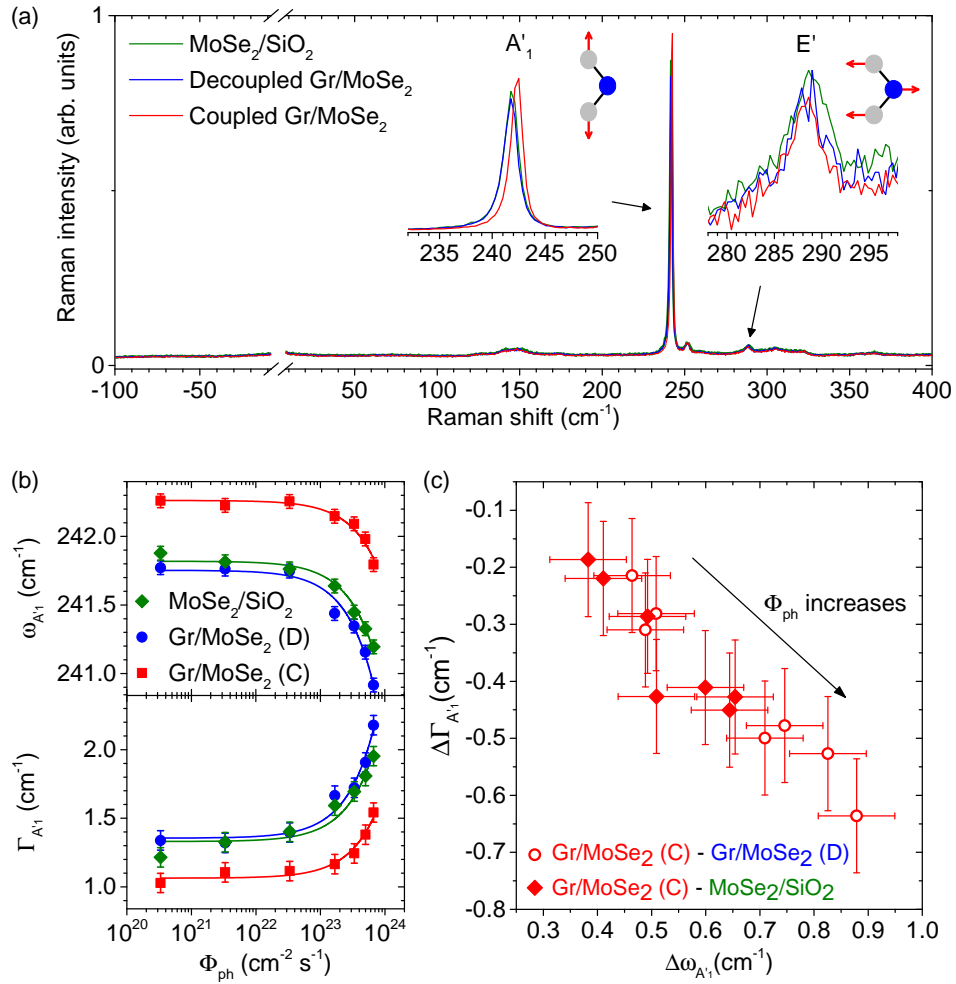


FIG. 4. (a) Raman spectra of MoSe₂ recorded at $\Phi_{\text{ph}} \approx 3.3 \times 10^{22} \text{ cm}^{-2} \text{ s}^{-1}$ for MoSe₂/SiO₂ (green), coupled (C, in red) and decoupled (D, in blue) Gr/MoSe₂. The insets show a close-up on the two one-phonon Raman-active modes in single-layer MoSe₂, namely the A'_1 and E' modes. The corresponding atomic displacements are sketched. (b) Extracted frequency (top) and FWHM (bottom) of the A'_1 -mode feature as a function of incident photon flux Φ_{ph} for MoSe₂/SiO₂ (green diamonds), coupled (red squares) and decoupled (blue circles) Gr/MoSe₂. The solid lines are linear fits. (c) Difference between the A'_1 -mode FWHMs $\Delta\Gamma_{A'_1}$ as a function of the difference between the A'_1 -mode frequencies $\Delta\omega_{A'_1}$ for coupled and decoupled Gr/MoSe₂ (open circles), and for coupled Gr/MoSe₂ and MoSe₂/SiO₂ (filled diamonds). All measurements were performed in ambient air.

sence of measurable phonon softening at high Φ_{ph} , indicates that the laser-induced temperature rise remains below $\sim 100 \text{ K}$ [69].

Second, for coupled Gr/MoSe₂, ω_{G} distinctly rises as Φ_{ph} increases, whereas Γ_{G} decreases (see Figs. 3(a)-(c)). Additionally, $I_{2\text{D}}/I_{\text{G}}$ (Figs. 3(e)) drops significantly. These spectroscopic features provide strong evidence for *photoinduced* ICT from MoSe₂ to graphene [47, 48]. We can now identify the sign of the net transferred charge flow using the correlation between $\omega_{2\text{D}}$ and ω_{G} in Fig. 3(f) as in Ref. 48 and 55. As Φ_{ph} increases, the data for Gr/SiO₂ and decoupled Gr/MoSe₂ show no clear correlations. In contrast, on coupled Gr/MoSe₂ $\omega_{2\text{D}}$ and ω_{G} display a linear correlation with a slope of ≈ 0.11 , a

value that clearly points towards photoinduced electron doping in graphene [48].

Using well-established theoretical modelling of electron-phonon coupling in doped graphene [46, 70], we quantitatively determine the Fermi energy of graphene relative to the Dirac point E_{F}^{Gr} or equivalently its doping level n_{Gr} . The values of E_{F}^{Gr} and n_{Gr} extracted from a global fitting procedure (see Ref. 48) are plotted in Fig. 3(f). As further discussed in Sec. V, E_{F}^{Gr} (n_{Gr}) saturates as Φ_{ph} increases and reaches up to $\approx 280 \text{ meV}$ ($\approx 5 \times 10^{12} \text{ cm}^{-2}$).

B. Hole accumulation in MoSe₂

Net electron transfer to graphene naturally implies hole accumulation in MoSe₂ and we now consider the high-resolution Raman response of MoSe₂. Figure 4(a) shows the MoSe₂ Raman spectra from MoSe₂/SiO₂, decoupled and coupled Gr/MoSe₂. In addition to several higher-order resonant features involving finite momentum phonons, one can identify the two Raman-active one-phonon modes in monolayer MoSe₂ with A'_1 symmetry (near 242 cm⁻¹) and E' symmetry (near 289 cm⁻¹) [71, 72]. The faint E' mode-feature is slightly downshifted on coupled Gr/MoSe₂, as compared to MoSe₂/SiO₂. The prominent A'_1 -mode feature is much similar for MoSe₂/SiO₂ and decoupled Gr/MoSe₂, but distinctively blueshifts (by ≈ 0.5 cm⁻¹) and gets narrower (by $\approx 20\%$) for coupled Gr/MoSe₂ (see Fig. 4(b)).

As in the case of graphene, changes in the Raman spectra can tentatively be assigned to doping, with possible spurious contributions from native strain and laser-induced heating. Interestingly, recent Raman studies in MoS₂ monolayers have demonstrated that the A'_1 -mode phonon undergoes modest doping-induced phonon renormalization, namely a downshift and a broadening for increasing electron concentration whereas the E' -mode phonon is largely insensitive to doping [50, 51]. Conversely, also in MoS₂, it was shown that under tensile (resp. compressive) strain the E' -mode feature undergoes much larger shifts than the A'_1 -mode feature [72, 73]. The A'_1 and E' phonons may thus be used as probes of ICT and strain, respectively. Based on these considerations, the minute E' phonon softening observed irrespective of Φ_{ph} in Gr/MoSe₂ relative to MoSe₂/SiO₂ suggests a slightly larger native tensile strain on Gr/MoSe₂, that has no impact whatsoever on ICT (see Supplemental Material [52], Fig. S4-S8). More importantly, the upshifted and narrower A'_1 -mode feature consistently observed up to $\Phi_{\text{ph}} \approx 6 \times 10^{23}$ cm⁻² s⁻¹ in coupled Gr/MoSe₂ indicates a lower electron density in MoSe₂ than in decoupled Gr/MoSe₂ and MoSe₂/SiO₂.

However, on the three regions of the sample, the frequency and FWHM of the A'_1 -mode feature downshifts and increases linearly as Φ_{ph} augments, respectively. Such trends counter-intuitively suggest photoinduced electron doping in MoSe₂. We tentatively assign the observed evolution of the A'_1 -mode feature to slight laser-induced temperature increase (estimated below 100 K [74] at $\Phi_{\text{ph}} \approx 6 \times 10^{23}$ cm⁻² s⁻¹), possibly combined with related photogating effects involving the presence of molecular adsorbates and trapped charges both acting as electron acceptors and laser-assisted desorption of the latter [51]. Remarkably, as shown in Fig. 4(c), the difference between the A'_1 frequencies (FWHM) measured on coupled Gr/MoSe₂ and decoupled Gr/MoSe₂ or MoSe₂/SiO₂ monotonically increases (decreases) as Φ_{ph} augments. These observations correspond to a *net photoinduced hole doping* for MoSe₂ in coupled Gr/MoSe₂, relative to decoupled Gr/MoSe₂ and MoSe₂/SiO₂, consis-

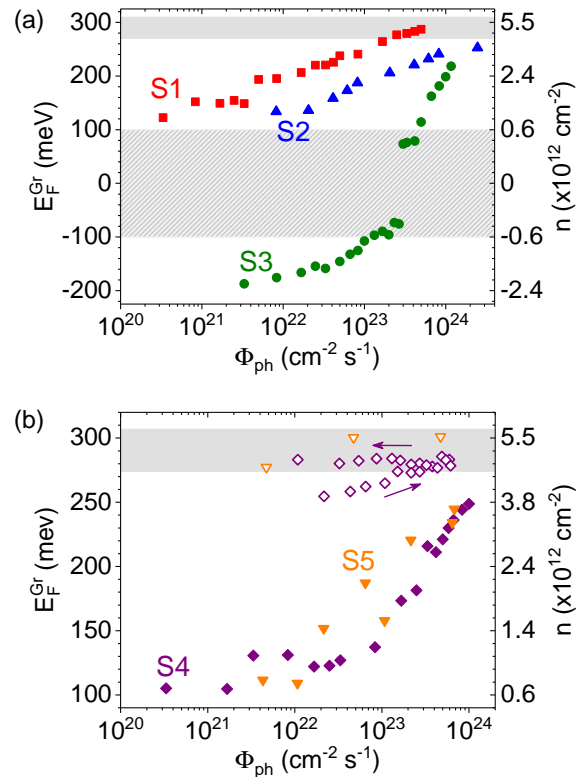


FIG. 5. (a) Fermi energy E_F^{Gr} (left) and doping level n_{Gr} (right) in graphene as a function of the incident photon flux Φ_{ph} . Measurements on three selected Gr/MoSe₂ samples (denoted S₁, S₂ and S₃) are represented with different symbols. The data shown in Fig. 1-4 is from S₁. The hatched region denotes the range of E_F^{Gr} close to the charge neutrality point where there is an uncertainty on the sign and on the exact value of E_F^{Gr} . The gray rectangle illustrates the saturation value of E_F^{Gr} . (b) E_F^{Gr} (left) and n_{Gr} (right) as a function of Φ_{ph} obtained under ambient conditions (filled symbols) and in vacuum (open symbols) at the same point of a Gr/MoSe₂/SiO₂ and a MoSe₂/Gr/SiO₂ heterostructure, denoted S₄ and S₅, respectively. Measurements under vacuum in S₄ are shown as Φ_{ph} is swept forward for the first time and then backward (see arrows).

tently with the net photoinduced electron transfer from MoSe₂ to graphene demonstrated in Fig. 3.

V. ENVIRONMENTAL EFFECTS

The charge density and exciton dynamics in 2D materials are known to be influenced by environmental effects, in particular by molecular adsorbates and the underlying substrate [49, 51, 75, 76]. To determine the generality of the results presented above, we compare in Fig. 5(a,b) the evolution of E_F^{Gr} with increasing Φ_{ph} recorded in ambient air and under high vacuum ($\lesssim 10^{-4}$ mbar) for a set of five samples, wherein strong PL quenching has also been

observed (see Supplemental Material [52], Fig. S11). Remarkably, all samples display (i) different initial doping at low Φ_{ph} , (ii) distinct sub-linear rises of E_F^{Gr} with increasing Φ_{ph} and (iii) similar saturation at a maximum E_F^{Gr} around 290 ± 15 meV (i.e., $n_{Gr} \approx 5 \times 10^{12} \text{ cm}^{-2}$). Interestingly, under vacuum, we systematically observe a transient regime with a photoinduced rise of E_F^{Gr} (at fixed Φ_{ph}) towards a saturation value that is attained on a rather long timescale (typically several minutes, depending on Φ_{ph} , see Fig. 5(b) and Supplemental Material [52], Fig. S10). Once E_F^{Gr} has reached its saturation value, E_F^{Gr} becomes independent on Φ_{ph} .

The distinct charge transfer dynamics observed under ambient conditions and in vacuum shed light on the role of molecular adsorbates at the surface of the vdWH. In vacuum, a significant fraction of the molecular adsorbates that lie on graphene are removed, including through laser-assisted desorption. These adsorbates are efficient electron traps [49, 51, 75], acting against the net photoinduced electron transfer from MoSe₂ to graphene. In the absence of molecular adsorbates, the electrons that are transferred from MoSe₂ to graphene remain on graphene as long as the laser illumination is on (see Sec. VI), leading to a saturation at a much lower Φ_{ph} as seen in Fig. 5(b). Such extrinsic effects have a strong impact on the optoelectronic response of 2DM and vdWH - most often examined under ambient conditions - and therefore provide an impetus for further studies under controlled atmospheres [49], using different substrates, stacking sequences and encapsulating materials [61–63]. Along this line, we have also studied (see Fig. 5(b) and Supplemental Material [52], Fig. S11) a MoSe₂/Gr/SiO₂ vdWH. Remarkably, the results obtained on this *inverted* heterostructure are very similar to those obtained in Gr/MoSe₂/SiO₂ vdWHs.

Finally, we have also compared the PL in Gr/MoSe₂/SiO₂ and MoSe₂/Gr/SiO₂ in ambient air and under vacuum conditions. While the PL of bare MoSe₂ is -as previously reported [75]- quenched under vacuum, the PL intensity and lineshape measured as a function of Φ_{ph} in ambient air and under vacuum in Gr/MoSe₂ are not appreciably different (See Fig. 6 and Supplemental Material [52], Fig. S12).

VI. DISCUSSION

A. Charge transfer mechanism

Let us first discuss ICT. Since the Dirac point of graphene is located between the valence band maximum and the conduction band minimum of MoSe₂ [77–79], the tunneling of photoexcited electrons *and* holes to graphene can be envisioned as long as energy and momentum are conserved and that E_F^{Gr} lies sufficiently below (above) the conduction band minimum (valence band maximum) of MoSe₂. Electron and hole transfer to graphene are sketched in Fig. 7(a,b). To account for our

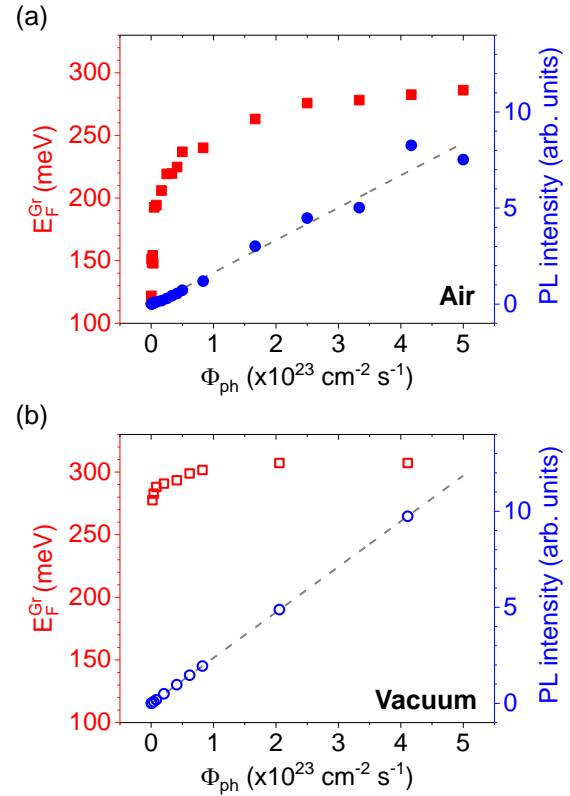


FIG. 6. Comparison between the dependence of E_F^{Gr} (left axis, red) and I_{PL}^A (right axis, blue) on Φ_{ph} measured on sample S2 (a) in ambient air and (b) in vacuum.

experimental findings, we propose the following scenario.

The band structure of coupled Gr/MoSe₂ can be, in first approximation, considered as the superposition of the bands of the different materials [23, 80] separated by a subnanometer “van der Waal gap”. The relative position of the band structure is determined by the offsets between the Dirac point of graphene and the valence (conduction) band maximum (minimum) of MoSe₂. In the dark, without loss of generality we may assume that both graphene and MoSe₂ are quasi-neutral. When visible light is shined onto Gr/MoSe₂, electron-hole pairs and excitons are mainly created in MoSe₂ since the latter absorbs significantly more than graphene [27, 54]. At this point, given the very similar electron and hole effective masses in MoSe₂ [81], the rates of photoinduced electron and hole transfer from MoSe₂ to graphene will chiefly depend on the the wavefunction overlap, the density of states in graphene and the energy difference between the band extrema in MoSe₂ and E_F^{Gr} .

Assuming the Dirac point lies closer to the valence band maximum than to the conduction band minimum [77, 78], the photoinduced electron current to graphene should exceed the hole current immediately after sample illumination, consistently with our experimental findings. Due to the small density of states of

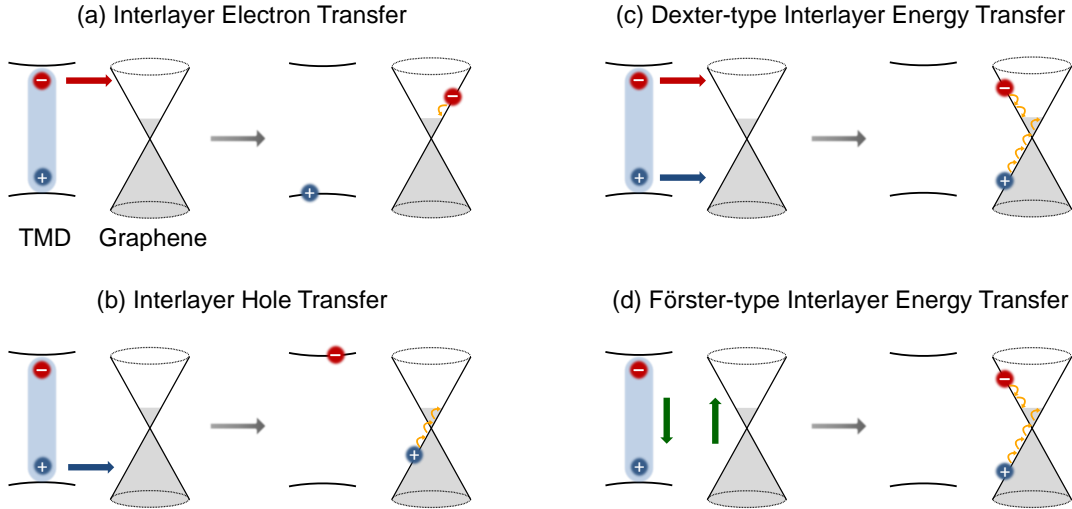


FIG. 7. Sketches, in momentum-energy space, of interlayer charge transfer (a,b), Dexter-type (c) and Förster-type (d) energy transfer processes from atomically thin TMD to graphene. Band-edge (A) excitons are symbolized by the blue shaded area with electron in red and hole in dark blue. The curved dark yellow arrows represent ultrafast energy relaxation of transferred carriers in graphene down to the Fermi level. In the case of balanced electron and hole flows to graphene, the charge transfer processes effectively result in energy transfer.

graphene near its Dirac point [12], the net electron transfer to graphene induces a sizeable rise of E_F^{Gr} above the Dirac point. Thus, as E_F^{Gr} moves away from the valence band maximum in MoSe₂, the hole current to n -doped graphene increases significantly. At sufficiently high Φ_{ph} , the vanishing of the net electron transfer to graphene then results from the cancellation of the photoinduced electron (Fig. 7(a)) and hole (Fig. 7(b)) currents. Note that our results in ambient air strongly suggest that electrons may escape from graphene (in Gr/MoSe₂/SiO₂) or MoSe₂ (in Gr/MoSe₂/SiO₂) resulting in a steady state reached at much higher Φ_{ph} than in vacuum and possibly at a E_F^{Gr} below the saturation value observed in vacuum (see Fig. 5(b)).

The very similar saturation values of E_F^{Gr} observed on several Gr/MoSe₂ samples (see Fig. 5(a,b)) both in ambient air *and* in vacuum suggest an intrinsic limit imposed by the band offsets between graphene and MoSe₂, as well as the electron and hole tunnelling efficiencies. Let us note, however, that the saturation value of E_F^{Gr} may also be affected by extrinsic factors, such as the presence of band tails states as well as other traps and defects. For instance in the case of n -doped MoSe₂, valence band tail states may lead to efficient hole trapping [82], hindering hole transfer to graphene and leading to saturation at larger E_F^{Gr} , closer to the conduction band minimum of MoSe₂. Additional experimental studies and modelling of photoinduced charge transfer using other TMDs with distinct band offsets relative to graphene will help determine whether the observed saturation has an intrinsic or extrinsic origin.

B. Impact of excitonic effects

Although our PL measurements make it clear that excitons are formed in MoSe₂, our discussion has so far overlooked the impact of excitonic effects on interlayer coupling. Upon optical excitation well-beyond the optical bandgap (as it is the case here), free electron-hole pairs *and* tightly bound excitons [59, 61] can be formed in Gr/MoSe₂. Despite exciton formation being highly efficient and occurring on sub-picosecond to a few picosecond timescales [67, 83], our PL measurements have also revealed equally short A (and B) exciton lifetimes in Gr/MoSe₂ (see Fig 2). Therefore the observed interlayer coupling processes may certainly involve band-edge excitons but may also imply direct *hot* carrier and/or exciton transfer to graphene. To assess the contribution of out of equilibrium effects, we have performed PL and Raman measurements in ambient air and in vacuum on a Gr/WS₂/SiO₂ vdWH at two different laser photon energies near the B exciton (2.33 eV) and slightly below the A exciton (1.96 eV). In the latter case only A excitons can be formed by means of an upconversion process [84, 85] (see Supplemental Material [52], Fig. S14). For both incoming photon energies, we observe strong PL quenching as well as photoinduced doping, very similar to the observations discussed above for Gr/MoSe₂ vdWHs. These findings indicate that ICT and IET processes mainly involve band-edge excitons. This conclusion is consistent with the fact that momentum conservation can be more easily fulfilled for an exciton than for a free charge carrier. Indeed, an exciton in the TMD can decay by transferring an electron or hole to a finite momentum state graphene

leaving the other carrier in the TMD with the excess momentum (see Fig. 7(a,b)), whereas at room temperature, a free charge carrier near the band-edges would need extra momentum provided by defect or phonon scattering.

C. Charge vs energy transfer

Finally, we address the competition between ICT and IET. Let us first emphasize that Raman measurements probe the steady state charge carrier densities in our samples and do not make it possible to extract ICT rates. Figure 6 summarizes our findings by confronting the dependence of E_F^{Gr} and I_{PL}^{A} on Φ_{ph} in sample S_2 . A crucial implication of our combined PL and Raman study is that the A and B exciton lifetimes in Gr/MoSe_2 are independent on Φ_{ph} and completely unaffected by the presence (in air, at low Φ_{ph}) or absence (in vacuum at any Φ_{ph} , and in air at high Φ_{ph}) of a *net* photoinduced ICT (here, electron transfer from MoSe_2 to graphene) (see also Supplemental Material [52], Fig. S13). Although balanced electron and hole transfer may contribute to PL quenching (see Fig. 7(a,b)), the data in Fig. 6 suggest that IET, either through electron exchange (i.e., a Dexter-type IET, Fig. 7(c)) or through dipole-dipole interaction (Förster-type IET, Fig. 7(d)) largely contributes to the massive PL quenching in Gr/MoSe_2 . Let us emphasize that although balanced ICT and Dexter-type IET follow *a priori* two distinct microscopic mechanisms (see Fig. 7(a-c)), both processes imply charge tunnelling (i.e., wavefunction overlap) and result in a similar final state where the energy of an exciton population is transferred to graphene. Interestingly, it was recently predicted in porphyrin-graphene hybrids that Dexter-type ET is largely inefficient compared to Förster-type ET event at sub-nanometer distances [86]. Further investigations of exciton dynamics in Gr/TMD as a function of temperature and of the GR-TMD distance should help confirm whether Förster-type IET is the dominant interlayer coupling mechanism in these intriguing heterointerfaces.

VII. CONCLUSION AND OUTLOOK

Using a combination of micro-Raman and photoluminescence spectroscopies, we have provided a comprehensive and quantitative characterization of the fingerprints of interlayer coupling in graphene-TMD heterostructures, namely, massive photoluminescence quenching and photoinduced doping. These observations are extremely reproducible and seemingly independent on the random rotational mismatch between graphene and the TMD monolayer.

As compared to electron transport measurements, micro-optical spectroscopy is contactless and allows spatially-resolved investigations of interlayer coupling. As an illustrative example, on a same sample we have shown that the electron transfer observed from MoSe_2 to

a tightly coupled graphene layer vanishes for a van der Waals gap as small as a few nm. This observation confirms the short range character of the interlayer charge transfer processes.

Our work invites applications for spatially-resolved photodoping of graphene since photoinduced doping levels as high as $5 \times 10^{12} \text{ cm}^{-2}$ – similar to those obtained using conventional gate dielectrics – can be reached without applying any external field. Although measurements of the graphene Raman modes certainly provide the most distinctive hallmark of photoinduced doping, the Raman response of the TMD layer also displays convincing evidence for interlayer charge transfer. As a result, Raman spectroscopy is an appealing technique to probe charge transfer and interlayer excitons in type II TMD/TMD heterostructures [32–36].

In addition, the observation of a seemingly universal saturation value of E_F^{Gr} paves the way towards all-optical investigations of band offsets in van der Waals heterostructures. Combined electron transport [87], angle-resolved photoemission [23, 79] and optical measurements should unveil the impact of strong bandgap renormalization and exciton binding energy in TMDs on their optoelectronic properties. Such developments also imply a deeper understanding of the microscopic charge transfer mechanisms.

Finally, the Gr/TMD system was also studied as a key building block in emerging optoelectronic nanodevices. In the absence of any applied external field, we demonstrate that excitons in TMD-coupled to graphene have an extremely short ($\sim 1 \text{ ps}$) lifetime, below the recently measured photoresponse time in photodetectors based on graphene and few-layer TMDs [20]. Intrinsically efficient interlayer coupling mechanisms leads to fast energy transfer from TMDs to graphene, followed by possibly even faster carrier relaxation down to the Fermi level of graphene [88, 89], limiting the performance of optoelectronic devices based on such van der Waals heterostructures. Therefore, our work provides an impetus for further engineering charge and exciton transport in two-dimensional optoelectronic devices.

EXPERIMENTAL DETAILS

Gr/MoSe_2 vdWHs were prepared onto Si wafers covered with a 90 nm thick SiO_2 epilayer using a viscoelastic transfer technique [90]. The Gr/MoSe_2 vdWHs were first characterized by atomic force microscopy (AFM) and then by micro-PL and micro-Raman measurements. As-prepared samples (such as sample S_1 discussed above, see Fig. 1(a)) as well as annealed samples (1 hour at 150°C and 2 hours at 200°C in high vacuum) such as sample S_3 were studied. Although more “pockets” (see Supplemental Material [52], Fig. S1) are present on as-prepared samples, we could observe, both in annealed and as-prepared samples, extended ($> 25 \mu\text{m}^2$) *coupled* Gr/MoSe_2 domains with smooth and uniform interfaces

due to a self-cleaning process [11].

PL and Raman studies were carried out in ambient air and in high vacuum, in a backscattering geometry, using a home-built confocal microscope. Unless otherwise noted, the samples were optically excited using a single longitudinal mode, linearly polarized, 2.33 eV (532 nm) continuous wave laser. The collected light was dispersed onto a charged-coupled device (CCD) array by a single (500 nm in focal length) monochromator equipped with a 150 (resp. 900 for graphene, 2400 for MoSe₂) grooves/mm grating for PL (resp. Raman) measurements. Spectral resolutions of 1.4 cm⁻¹ and 0.6 cm⁻¹ were obtained for Raman measurements with the 900 and 2400 grooves/mm grating, respectively. The sample holder was mounted onto a x-y-z piezoelectric stage, allowing hyperspectral imaging. Time-resolved PL measurements were performed on the same setup using a pulsed supercontinuum laser, with a repetition rate tunable from 1.95 MHz up to 78 MHz. The unpolarized output of the supercontinuum laser at 1.96 eV (633 nm) was selected using an acousto-optic tunable filter. PL decays were obtained using an avalanche photodiode coupled to a time-tagged, time-correlated single photon counting board. The incident photon flux Φ_{ph} is obtained by measuring the laser power and the area of the laser spot.

For instance, with a measured optical power of 1 μW at the objective at 2.33 eV, we obtain a photon flux of $2.2 \times 10^{21} \text{ cm}^{-2} \text{ s}^{-1}$ using a 100x objective with a numerical aperture of 0.9. The Raman peaks are fit using Lorentzian and modified Lorentzian [48, 56] profiles for the G- and 2D-mode features, respectively, and Voigt profiles (with a fixed Gaussian width taking into account our spectral resolution) for MoSe₂ features. Therefore in Fig. 4(b), the linewidth $\Gamma_{A'_1}$ has to be understood as the Lorentzian FWHM extracted from a Voigt fit.

ACKNOWLEDGMENTS

We thank D.M. Basko, C. Robert, D. Lagarde, X. Marie, and A. Ouerghi for fruitful discussions. We are grateful to J. Chrétien for his contribution to the experimental measurements, to H. Majjad and M. Rastei for help with AFM measurements, and to the StNano clean room staff and M. Romeo for technical assistance. We acknowledge financial support from the Agence Nationale de la Recherche (under grant H2DH ANR-15-CE24-0016) and from the LabEx NIE (under Grant ANR-11-LABX-0058-NIE within the Investissement d'Avenir program ANR-10-IDEX-0002-02). S.B. is a member of Institut Universitaire de France (IUF).

[1] Th Förster, “Zwischenmolekulare energiewanderung und fluoreszenz,” *Annalen der physik* **437**, 55 (1948).

[2] Rienk van Grondelle, Jan P. Dekker, Tomas Gillbro, and Villy Sundstrom, “Energy transfer and trapping in photosynthesis,” *Biochimica et Biophysica Acta (BBA) - Bioenergetics* **1187**, 1 – 65 (1994).

[3] Burak Guzelturk and Hilmi Volkan Demir, “Near-field energy transfer using nanoemitters for optoelectronics,” *Advanced Functional Materials* **26**, 8158–8177 (2016).

[4] Alexander Govorov, Pedro Ludwig Hernández Martínez, and Hilmi Volkan Demir, *Understanding and Modeling FRET* (Springer, 2016).

[5] Volkhard May and Oliver Kühn, *Charge and energy transfer dynamics in molecular systems* (John Wiley & Sons, 2008).

[6] Simon M Sze and Kwok K Ng, *Physics of semiconductor devices* (John Wiley & Sons, 2006).

[7] David L Dexter, “A theory of sensitized luminescence in solids,” *The Journal of Chemical Physics* **21**, 836–850 (1953).

[8] A. K. Geim and I. V. Grigorieva, “Van der Waals heterostructures,” *Nature* **499**, 419–425 (2013).

[9] KS Novoselov, A Mishchenko, A Carvalho, and AH Castro Neto, “2D materials and van der Waals heterostructures,” *Science* **353**, aac9439 (2016).

[10] Kin Fai Mak and Jie Shan, “Photonics and optoelectronics of 2D semiconductor transition metal dichalcogenides,” *Nat. Photonics* **10**, 216–226 (2016).

[11] SJ Haigh, A Gholinia, R Jalil, S Romani, L Britnell, DC Elias, KS Novoselov, LA Ponomarenko, AK Geim, and R Gorbachev, “Cross-sectional imaging of individual layers and buried interfaces of graphene-based heterostructures and superlattices,” *Nat. Mater.* **11**, 764–767 (2012).

[12] A. H. Castro Neto, F. Guinea, N. M. R. Peres, K. S. Novoselov, and A. K. Geim, “The electronic properties of graphene,” *Rev. Mod. Phys.* **81**, 109–162 (2009).

[13] Kin Fai Mak, Changgu Lee, James Hone, Jie Shan, and Tony F. Heinz, “Atomically Thin MoS₂: A New Direct-Gap Semiconductor,” *Phys. Rev. Lett.* **105**, 136805 (2010).

[14] Andrea Splendiani, Liang Sun, Yuanbo Zhang, Tianshu Li, Jonghwan Kim, Chi-Yung Chim, Giulia Galli, and Feng Wang, “Emerging Photoluminescence in Monolayer MoS₂,” *Nano Lett.* **10**, 1271–1275 (2010).

[15] Liam Britnell, RM Ribeiro, A Eckmann, R Jalil, BD Belle, A Mishchenko, Y-J Kim, RV Gorbachev, T Georgiou, SV Morozov, et al., “Strong light-matter interactions in heterostructures of atomically thin films,” *Science* **340**, 1311–1314 (2013).

[16] Woo Jong Yu, Yuan Liu, Hailong Zhou, Anxiang Yin, Zheng Li, Yu Huang, and Xiangfeng Duan, “Highly efficient gate-tunable photocurrent generation in vertical heterostructures of layered materials,” *Nat. Nanotechnol.* **8**, 952–958 (2013).

[17] Kallol Roy, Medini Padmanabhan, Srijit Goswami, T. Phanindra Sai, Gopalakrishnan Ramalingam, Srinivasan Raghavan, and Arindam Ghosh, “Graphene-MoS₂ hybrid structures for multifunctional photoresponsive memory devices,” *Nat. Nanotechnol.* **8**, 826–830 (2013).

[18] Wenjing Zhang, Chih-Piao Chuu, Jing-Kai Huang, Chang-Hsiao Chen, Meng-Lin Tsai, Yung-Huang Chang, Chi-Te Liang, Yu-Ze Chen, Yu-Lun Chueh, Jr-Hau He, Mei-Yin Chou, and Lain-Jong Li, "Ultrahigh-Gain Photodetectors Based on Atomically Thin Graphene-MoS₂ Heterostructures," *Sci. Rep.* **4** (2014), 10.1038/srep03826.

[19] Domenico De Fazio, Ilya Goykhman, Duhee Yoon, Matteo Bruna, Anna Eiden, Silvia Milana, Ugo Sassi, Matteo Barbone, Dumitru Dumcenco, Kolyo Marinov, Andras Kis, and Andrea C. Ferrari, "High responsivity, large-area graphene/MoS₂ flexible photodetectors," *ACS Nano* **10**, 8252–8262 (2016).

[20] M Massicotte, P Schmidt, F Vialla, KG Schädler, A Reserbat-Plantey, K Watanabe, T Taniguchi, KJ Tielrooij, and FHL Koppens, "Picosecond photoresponse in van der Waals heterostructures," *Nat. Nanotechnol.* **11**, 42–46 (2016).

[21] Kathleen M McCreary, Aubrey T Hanbicki, Jeremy T Robinson, Enrique Cobas, James C Culbertson, Adam L Friedman, Glenn G Jernigan, and Berend T Jonker, "Large-area synthesis of continuous and uniform MoS₂ monolayer films on graphene," *Adv. Funct. Mater.* **24**, 6449–6454 (2014).

[22] Gi Woong Shim, Kwonjae Yoo, Seung-Bum Seo, Jongwoo Shin, Dae Yool Jung, Il-Suk Kang, Chi Won Ahn, Byung Jin Cho, and Sung-Yool Choi, "Large-area single-layer MoSe₂ and its van der Waals heterostructures," *ACS Nano* **8**, 6655–6662 (2014).

[23] Debora Pierucci, Hugo Henck, José Avila, Adrian Balan, Carl H Naylor, Gilles Patriarche, Yannick J Dappe, Mathieu G Silly, Fausto Sirotti, AT Charlie Johnson, et al., "Band alignment and minibands in monolayer MoS₂-graphene van der Waals heterostructures," *Nano Lett.* (2016).

[24] Jiaqi He, Nardeep Kumar, Matthew Z Bellus, Hsin-Ying Chiu, Dawei He, Yongsheng Wang, and Hui Zhao, "Electron transfer and coupling in graphene–tungsten disulfide van der Waals heterostructures," *Nat. Commun.* **5** (2014).

[25] Hugo Henck, Debora Pierucci, Julien Chaste, Carl H. Naylor, Jose Avila, Adrian Balan, Mathieu G. Silly, Maria C. Asensio, Fausto Sirotti, A. T Charlie Johnson, Emmanuel Lhuillier, and Abdelkarim Ouerghi, "Electrolytic phototransistor based on graphene-mos₂ van der waals p-n heterojunction with tunable photoresponse," *Applied Physics Letters* **109**, 113103 (2016).

[26] FHL Koppens, T Mueller, Ph Avouris, AC Ferrari, MS Vitiello, and M Polini, "Photodetectors based on graphene, other two-dimensional materials and hybrid systems," *Nat. Nanotechnol.* **9**, 780–793 (2014).

[27] Kin Fai Mak, Long Ju, Feng Wang, and Tony F Heinz, "Optical spectroscopy of graphene: from the far infrared to the ultraviolet," *Solid State Commun.* **152**, 1341–1349 (2012).

[28] Klaas-Jan Tielrooij, Lukasz Piatkowski, Mathieu Massicotte, Achim Woessner, Qiong Ma, Yongjin Lee, Kevin Scott Myhro, Chun Ning Lau, Pablo Jarillo-Herrero, Niek F van Hulst, et al., "Generation of photo-voltage in graphene on a femtosecond timescale through efficient carrier heating," *Nat. Nanotechnol.* **10**, 437–443 (2015).

[29] Gang Wang, Alexey Chernikov, Mikhail M Glazov, Tony F Heinz, Xavier Marie, Thierry Amand, and Bernhard Urbaszek, "Excitons in atomically thin transition metal dichalcogenides," *arXiv preprint arXiv:1707.05863* (2017).

[30] Fengnian Xia, Han Wang, Di Xiao, Madan Dubey, and Ashwin Ramasubramaniam, "Two-dimensional material nanophotonics," *Nat. Photonics* **8**, 899–907 (2014).

[31] John R Schaibley, Hongyi Yu, Genevieve Clark, Pasqual Rivera, Jason S Ross, Kyle L Seyler, Wang Yao, and Xiaodong Xu, "Valleytronics in 2D materials," *Nature Reviews Materials* **1**, 16055 (2016).

[32] Frank Ceballos, Matthew Z Bellus, Hsin-Ying Chiu, and Hui Zhao, "Ultrafast charge separation and indirect exciton formation in a MoS₂–MoSe₂ van der Waals heterostructure," *ACS Nano* **8**, 12717–12724 (2014).

[33] Xiaoping Hong, Jonghwan Kim, Su-Fei Shi, Yu Zhang, Chenhao Jin, Yinghui Sun, Sefaattin Tongay, Junqiao Wu, Yanfeng Zhang, and Feng Wang, "Ultrafast charge transfer in atomically thin MoS₂/WS₂ heterostructures," *Nat. Nanotechnol.* **9**, 682–686 (2014).

[34] Hui Fang, Corsin Battaglia, Carlo Carraro, Slavomir Nemsak, Burak Ozdol, Jeong Seuk Kang, Hans A. Bechtel, Sujay B. Desai, Florian Kronast, Ahmet A. Unal, Giuseppina Conti, Catherine Conlon, Gunnar K. Palsson, Michael C. Martin, Andrew M. Minor, Charles S. Fadley, Eli Yablonovitch, Roya Maboudian, and Ali Javey, "Strong interlayer coupling in van der Waals heterostructures built from single-layer chalcogenides," *Proc. Natl. Acad. Sci. U. S. A.* **111**, 6198–6202 (2014).

[35] Chul-Ho Lee, Gwan-Hyoung Lee, Arend M. van der Zande, Wenchao Chen, Yilei Li, Minyong Han, Xu Cui, Ghidewon Arefe, Colin Nuckolls, Tony F. Heinz, Jing Guo, James Hone, and Philip Kim, "Atomically thin pn junctions with van der Waals heterointerfaces," *Nat. Nanotechnol.* **9**, 676–681 (2014).

[36] Pasqual Rivera, John R Schaibley, Aaron M Jones, Jason S Ross, Sanfeng Wu, Grant Aivazian, Philip Clement, Kyle Seyler, Genevieve Clark, Nirmal J Ghimire, et al., "Observation of long-lived interlayer excitons in monolayer MoSe₂–WSe₂ heterostructures," *Nat. Commun.* **6** (2015).

[37] Daichi Kozawa, Alexandra Carvalho, Ivan Verzhbitskiy, Francesco Giustiniano, Yuhei Miyauchi, Shinichiro Mouri, AH Castro Neto, Kazunari Matsuda, and Goki Eda, "Evidence for fast interlayer energy transfer in MoSe₂/WS₂ heterostructures," *Nano Lett.* (2016).

[38] Cyrielle Roquelet, Damien Garrot, Jean-Sébastien Lautret, Christophe Voisin, Valérie Alain-Rizzo, Ph Rousignol, JA Delaire, and Emmanuelle Deleporte, "Quantum efficiency of energy transfer in noncovalent carbon nanotube/porphyrin compounds," *Appl. Phys. Lett.* **97**, 141918 (2010).

[39] Zheyuan Chen, Stéphane Berciaud, Colin Nuckolls, Tony F Heinz, and Louis E Brus, "Energy transfer from individual semiconductor nanocrystals to graphene," *ACS Nano* **4**, 2964–2968 (2010).

[40] L Gaudreau, KJ Tielrooij, GEDK Prawiroatmodjo, J Osmond, FJ García de Abajo, and FHL Koppens, "Universal distance-scaling of nonradiative energy transfer to graphene," *Nano Lett.* **13**, 2030–2035 (2013).

[41] Julia Tisler, Thomas Oeckinghaus, Rainer J Sthir, Roman Kolesov, Rolf Reuter, Friedemann Reinhard, and Jörg Wrachtrup, "Single defect center scanning near-field optical microscopy on graphene," *Nano Lett.* **13**, 3152–3156 (2013).

[42] François Federspiel, Guillaume Froehlicher, Michel Nasilowski, Silvia Pedetti, Ather Mahmood, Bernard Doudin, Serin Park, Jeong-O Lee, David Halley, Benoît Dubertret, et al., “Distance dependence of the energy transfer rate from a single semiconductor nanostructure to graphene,” *Nano Lett.* **15**, 1252–1258 (2015).

[43] Ferry Prins, Aaron J Goodman, and William A Tisdale, “Reduced dielectric screening and enhanced energy transfer in single-and few-layer MoS₂,” *Nano Lett.* **14**, 6087–6091 (2014).

[44] Archana Raja, Andrs Montoya-Castillo, Johanna Zultak, Xiao-Xiao Zhang, Ziliang Ye, Cyrielle Roquelet, Daniel A Chenet, Arend M van der Zande, Pinshane Huang, Steffen Jockusch, et al., “Energy transfer from quantum dots to graphene and MoS₂: The role of absorption and screening in two-dimensional materials,” *Nano Lett.* **16**, 2328–2333 (2016).

[45] Jun Yan, Yuanbo Zhang, Philip Kim, and Aron Pinczuk, “Electric field effect tuning of electron-phonon coupling in graphene,” *Phys. Rev. Lett.* **98**, 166802 (2007).

[46] Simone Pisana, Michele Lazzeri, Cinzia Casiraghi, Kostya S. Novoselov, A. K. Geim, Andrea C. Ferrari, and Francesco Mauri, “Breakdown of the adiabatic born-oppenheimer approximation in graphene,” *Nat. Mater.* **6**, 198–201 (2007).

[47] A. Das, S. Pisana, B. Chakraborty, S. Pisanec, S. K. Saha, U. V. Waghmare, K. S. Novoselov, H. R. Krishnamurthy, A. K. Geim, A. C. Ferrari, and A. K. Sood, “Monitoring dopants by Raman scattering in an electrochemically top-gated graphene transistor,” *Nat. Nanotechnol.* **3**, 210–215 (2008).

[48] Guillaume Froehlicher and Stéphane Berciaud, “Raman spectroscopy of electrochemically gated graphene transistors: Geometrical capacitance, electron-phonon, electron-electron, and electron-defect scattering,” *Phys. Rev. B* **91**, 205413 (2015).

[49] Sunmin Ryu, Li Liu, Stéphane Berciaud, Young-Jun Yu, Haitao Liu, Philip Kim, George W. Flynn, and Louis E. Brus, “Atmospheric oxygen binding and hole doping in deformed graphene on a SiO₂ substrate,” *Nano Lett.* **10**, 4944–4951 (2010).

[50] Biswanath Chakraborty, Achintya Bera, D. V. S. Muthu, Somnath Bhowmick, U. V. Waghmare, and A. K. Sood, “Symmetry-dependent phonon renormalization in monolayer MoS₂ transistor,” *Phys. Rev. B* **85**, 161403 (2012).

[51] Bastian Miller, Eric Parzinger, Anna Vernickel, Alexander W Holleitner, and Ursula Wurstbauer, “Photogating of mono-and few-layer MoS₂,” *Appl. Phys. Lett.* **106**, 122103 (2015).

[52] See Supplemental Material for details on Atomic force microscopy, Raman spectra of graphene and MoSe₂ for increasing Φ_{ph} , details on spatially-resolved Raman studies, additional photoluminescence and Raman measurements, discussion on the frequency of the Raman 2D-mode feature in Gr/MoSe₂, discussion on optical interference effects.

[53] Andrea C. Ferrari and Denis M. Basko, “Raman spectroscopy as a versatile tool for studying the properties of graphene,” *Nat. Nanotechnol.* **8**, 235–246 (2013).

[54] Yilei Li, Alexey Chernikov, Xian Zhang, Albert Rigosi, Heather M. Hill, Arend M. van der Zande, Daniel A. Chenet, En-Min Shih, James Hone, and Tony F. Heinz, “Measurement of the optical dielectric function of monolayer transition-metal dichalcogenides: MoS₂, MoSe₂, WS₂, and WSe₂,” *Phys. Rev. B* **90**, 205422 (2014).

[55] Ji Eun Lee, Gwanghyun Ahn, Jihye Shim, Young Sik Lee, and Sunmin Ryu, “Optical separation of mechanical strain from charge doping in graphene,” *Nat. Commun.* **3**, 1024 (2012).

[56] Dominik Metten, François Federspiel, Michelangelo Romeo, and Stéphane Berciaud, “All-optical blister test of suspended graphene using micro-Raman spectroscopy,” *Phys. Rev. Appl.* **2**, 054008 (2014).

[57] Gwanghyun Ahn, Hye Ri Kim, Taeg Yeoung Ko, Kyounghun Choi, Kenji Watanabe, Takashi Taniguchi, Byung Hee Hong, and Sunmin Ryu, “Optical probing of the electronic interaction between graphene and hexagonal boron nitride,” *ACS Nano* **7**, 1533–1541 (2013).

[58] F. Forster, A. Molina-Sanchez, S. Engels, A. Epping, K. Watanabe, T. Taniguchi, L. Wirtz, and C. Stampfer, “Dielectric screening of the Kohn anomaly of graphene on hexagonal boron nitride,” *Phys. Rev. B* **88**, 085419 (2013).

[59] Miguel M. Ugeda, Aaron J. Bradley, Su-Fei Shi, Felipe H. da Jornada, Yi Zhang, Diana Y. Qiu, Wei Ruan, Sung-Kwan Mo, Zahid Hussain, Zhi-Xun Shen, Feng Wang, Steven G. Louie, and Michael F. Crommie, “Giant bandgap renormalization and excitonic effects in a monolayer transition metal dichalcogenide semiconductor,” *Nat. Mater.* **5**, 1091 (2014).

[60] Andreas V Stier, Nathan P Wilson, Genevieve Clark, Xiaodong Xu, and Scott A Crooker, “Probing the influence of dielectric environment on excitons in monolayer WSe₂: Insight from high magnetic fields,” *Nano Letters* **16**, 7054–7060 (2016).

[61] Archana Raja, Andrey Chaves, Jaeeun Yu, Ghidewon Arefe, Heather M Hill, Albert F Rigosi, Timothy C Berkelbach, Philipp Nagler, Christian Schüller, Tobias Korn, et al., “Coulomb engineering of the bandgap and excitons in two-dimensional materials,” *Nature Communications* **8**, 15251 (2017).

[62] F. Cadiz, E. Courtade, C. Robert, G. Wang, Y. Shen, H. Cai, T. Taniguchi, K. Watanabe, H. Carrere, D. Lagarde, M. Manca, T. Amand, P. Renucci, S. Tongay, X. Marie, and B. Urbaszek, “Excitonic linewidth approaching the homogeneous limit in mos₂-based van der waals heterostructures,” *Phys. Rev. X* **7**, 021026 (2017).

[63] Obafunso A Ajai, Jenny V Ardelean, Gabriella D Shepard, Jue Wang, Abhinandan Antony, Takeshi Taniguchi, Kenji Watanabe, Tony F Heinz, Stefan Strauf, X-Y Zhu, and James C Hone, “Approaching the intrinsic photoluminescence linewidth in transition metal dichalcogenide monolayers,” *2D Materials* **4**, 031011 (2017).

[64] Nardeep Kumar, Qiannan Cui, Frank Ceballos, Dawei He, Yongsheng Wang, and Hui Zhao, “Exciton-exciton annihilation in MoSe₂ monolayers,” *Phys. Rev. B* **89**, 125427 (2014).

[65] Shinichiro Mouri, Yuhei Miyazaki, Minglin Toh, Weijie Zhao, Goki Eda, and Kazunari Matsuda, “Nonlinear photoluminescence in atomically thin layered WSe₂ arising from diffusion-assisted exciton-exciton annihilation,” *Phys. Rev. B* **90**, 155449 (2014).

[66] Hongyan Shi, Rusen Yan, Simone Bertolazzi, Jacopo Brivio, Bo Gao, Andras Kis, Debdeep Jena, Huili Grace Xing, and Libai Huang, “Exciton dynamics in suspended monolayer and few-layer mos2 2d crystals,” *ACS*

Nano **7**, 1072–1080 (2013).

[67] C. Robert, D. Lagarde, F. Cadiz, G. Wang, B. Lasagne, T. Amand, A. Balocchi, P. Renucci, S. Tongay, B. Urbaszek, and X. Marie, “Exciton radiative lifetime in transition metal dichalcogenide monolayers,” Phys. Rev. B **93**, 205423 (2016).

[68] Stéphane Berciaud, Sunmin Ryu, Louis E. Brus, and Tony F. Heinz, “Probing the intrinsic properties of exfoliated graphene: Raman spectroscopy of free-standing monolayers,” Nano Lett. **9**, 346–352 (2009).

[69] Alexander A Balandin, “Thermal properties of graphene and nanostructured carbon materials,” Nat. Mater. **10**, 569–581 (2011).

[70] Tsuneya Ando, “Anomaly of optical phonon in monolayer graphene,” J. Phys. Soc. Jpn. **75**, 124701 (2006).

[71] P. Soubelet, A. E. Bruchhausen, A. Fainstein, K. Nogajewski, and C. Faugeras, “Resonance effects in the Raman scattering of monolayer and few-layer MoSe₂,” Phys. Rev. B **93**, 155407 (2016).

[72] Xin Zhang, Xiao-Fen Qiao, Wei Shi, Jiang-Bin Wu, De-Sheng Jiang, and Ping-Heng Tan, “Phonon and Raman scattering of two-dimensional transition metal dichalcogenides from monolayer, multilayer to bulk material,” Chem. Soc. Rev. **44**, 2757 (2015).

[73] Hiram J. Conley, Bin Wang, Jed I. Ziegler, Richard F. Haglund, Sokrates T. Pantelides, and Kirill I. Bolotin, “Bandgap Engineering of Strained Monolayer and Bilayer MoS₂,” Nano Lett. **13**, 3626–3630 (2013).

[74] Dattatray J Late, Sharmila N Shirodkar, Umesh V Waghmare, Vinayak P Dravid, and CNR Rao, “Thermal expansion, anharmonicity and temperature-dependent Raman spectra of single-and few-layer MoSe₂ and WSe₂,” ChemPhysChem **15**, 1592–1598 (2014).

[75] Sefaattin Tongay, Jian Zhou, Can Ataca, Jonathan Liu, Jeong Seuk Kang, Tyler S Matthews, Long You, Jingbo Li, Jeffrey C Grossman, and Junqiao Wu, “Broad-range modulation of light emission in two-dimensional semiconductors by molecular physisorption gating,” Nano Lett. **13**, 2831–2836 (2013).

[76] Fabian Cadiz, Cedric Robert, Gang Wang, Wilson Kong, Xi Fan, Mark Blei, Delphine Lagarde, Maxime Gay, Marco Manca, Takashi Taniguchi, Kenji Watanabe, Thierry Amand, Xavier Marie, Pierre Renucci, Sefaattin Tongay, and Bernhard Urbaszek, “Ultra-low power threshold for laser induced changes in optical properties of 2d molybdenum dichalcogenides,” 2D Materials **3**, 045008 (2016).

[77] Young-Jun Yu, Yue Zhao, Sunmin Ryu, Louis E Brus, Kwang S Kim, and Philip Kim, “Tuning the graphene work function by electric field effect,” Nano Lett. **9**, 3430–3434 (2009).

[78] Yufeng Liang, Shouting Huang, Ryan Soklaski, and Li Yang, “Quasiparticle band-edge energy and band offsets of monolayer of molybdenum and tungsten chalcogenides,” Appl. Phys. Lett. **103**, 042106 (2013).

[79] Neil R. Wilson, Paul V. Nguyen, Kyle Seyler, Pasqual Rivera, Alexander J. Marsden, Zachary P. L. Laker, Gabriel C. Constantinescu, Viktor Kandyba, Alexei Barinov, Nicholas D. M. Hine, Xiaodong Xu, and David H. Cobden, “Determination of band offsets, hybridization, and exciton binding in 2D semiconductor heterostructures,” Science Advances **3** (2017), 10.1126/sciadv.1601832.

[80] K. Kośmider and J. Fernández-Rossier, “Electronic properties of the MoS₂-WS₂ heterojunction,” Phys. Rev. B **87**, 075451 (2013).

[81] Andor Kormnyos, Guido Burkard, Martin Gmitra, Jaroslav Fabian, Viktor Zlyomi, Neil D Drummond, and Vladimir Falko, “k p theory for two-dimensional transition metal dichalcogenide semiconductors,” 2D Materials **2**, 022001 (2015).

[82] Marco M. Furchi, Andreas Pospischil, Florian Libisch, Joachim Burgdorfer, and Thomas Mueller, “Photovoltaic Effect in an Electrically Tunable van der Waals Heterojunction,” Nano Lett. **14**, 4785–4791 (2014).

[83] Philipp Steinleitner, Philipp Merkl, Philipp Nagler, Joshua Mornhinweg, Christian Schller, Tobias Korn, Alexey Chernikov, and Rupert Huber, “Direct observation of ultrafast exciton formation in a monolayer of wse₂,” Nano Letters **17**, 1455–1460 (2017).

[84] Aaron M Jones, Hongyi Yu, John R Schaibley, Jiaqiang Yan, David G Mandrus, Takashi Taniguchi, Kenji Watanabe, Hanan Dery, Wang Yao, and Xiaodong Xu, “Excitonic luminescence upconversion in a two-dimensional semiconductor,” Nat. Phys. **12**, 323–327 (2016).

[85] Thibault Chervy, Stefano Azzini, Etienne Lorchat, Shaojun Wang, Yuri Gorodetski, James A Hutchison, Stéphane Berciaud, Thomas W Ebbesen, and Cyriaque Genet, “Spin-momentum locked polariton transport in the chiral strong coupling regime,” arXiv preprint arXiv:1701.07972 (2017).

[86] Ermin Malic, Heiko Appel, Oliver T Hofmann, and Angel Rubio, “Förster-induced energy transfer in functionalized graphene,” The Journal of Physical Chemistry C **118**, 9283–9289 (2014).

[87] Kyounghwan Kim, Stefano Larentis, Babak Fallahazad, Kayoung Lee, Jiamin Xue, David C Dillen, Chris M Corbet, and Emanuel Tutuc, “Band alignment in WSe₂-graphene heterostructures,” ACS Nano **9**, 4527–4532 (2015).

[88] Jens Christian Johannsen, Søren Ulstrup, Federico Cilento, Alberto Crepaldi, Michele Zacchigna, Cephise Cacho, I. C. Edmond Turcu, Emma Springate, Felix Fromm, Christian Raidel, Thomas Seyller, Fulvio Parmigiani, Marco Grioni, and Philip Hofmann, “Direct view of hot carrier dynamics in graphene,” Phys. Rev. Lett. **111**, 027403 (2013).

[89] Isabella Gierz, Jesse C Petersen, Matteo Mitrano, Cephise Cacho, IC Edmond Turcu, Emma Springate, Alexander Stöhr, Axel Köhler, Ulrich Starke, and Andrea Cavalleri, “Snapshots of non-equilibrium dirac carrier distributions in graphene,” Nature materials **12**, 1119–1124 (2013).

[90] Andres Castellanos-Gomez, Michele Buscema, Rianda Molenaar, Vibhor Singh, Laurens Janssen, Herre S J van der Zant, and Gary A Steele, “Deterministic transfer of two-dimensional materials by all-dry viscoelastic stamping,” 2D Mater. **1**, 011002 (2014).

[91] AV Kretinin, Y Cao, JS Tu, GL Yu, R Jalil, KS Novoselov, SJ Haigh, A Gholinia, A Mishchenko, M Lozada, et al., “Electronic properties of graphene encapsulated with different two-dimensional atomic crystals,” Nano Lett. **14**, 3270–3276 (2014).

[92] D. M. Basko, “Theory of resonant multiphonon Raman scattering in graphene,” Phys. Rev. B **78**, 125418 (2008).

[93] Stéphane Berciaud, Xianglong Li, Han Htoon, Louis E.

Brus, Stephen K. Doorn, and Tony F. Heinz, "Intrinsic line shape of the Raman 2D-mode in freestanding graphene monolayers," *Nano Lett.* **13**, 3517 (2013).

[94] Nobuhiko Mitoma, Ryo Nouchi, and Katsumi Tanigaki, "Photo-oxidation of graphene in the presence of water," *The Journal of Physical Chemistry C* **117**, 1453–1456 (2013).

[95] J. Maultzsch, S. Reich, and C. Thomsen, "Double-resonant Raman scattering in graphite: Interference effects, selection rules, and phonon dispersion," *Phys. Rev. B* **70**, 155403 (2004).

[96] Pedro Venezuela, Michele Lazzari, and Francesco Mauri, "Theory of double-resonant Raman spectra in graphene: Intensity and line shape of defect-induced and two-phonon bands," *Phys. Rev. B* **84**, 035433 (2011).

[97] Hannu-Pekka Komsa and Arkady V. Krasheninnikov, "Electronic structures and optical properties of realistic transition metal dichalcogenide heterostructures from first principles," *Phys. Rev. B* **88**, 085318 (2013).

[98] Duhee Yoon, Hyerim Moon, Young-Woo Son, Jin Sik Choi, Bae Ho Park, Young Hun Cha, Young Dong Kim, and Hyeonsik Cheong, "Interference effect on Raman spectrum of graphene on SiO₂/Si," *Phys. Rev. B* **80**, 125422 (2009).

[99] Song-Lin Li, Hisao Miyazaki, Haisheng Song, Hiromi Kuramochi, Shu Nakaharai, and Kazuhito Tsukagoshi, "Quantitative Raman spectrum and reliable thickness identification for atomic layers on insulating substrates," *ACS Nano* **6**, 7381–7388 (2012).

[100] Michele Buscema, Gary A Steele, Herre SJ van der Zant, and Andres Castellanos-Gomez, "The effect of the substrate on the raman and photoluminescence emission of single-layer MoS₂," *Nano Res.* **7**, 561–571 (2014).

[101] Guillaume Froehlicher, Etienne Lorchat, and Stéphane Berciaud, "Direct versus indirect band gap emission and exciton-exciton annihilation in atomically thin molybdenum ditelluride (MoTe₂)," *Phys. Rev. B* **94**, 085429 (2016).

Supplemental Material

S1. ADDITIONAL RESULTS ON SAMPLE S₁

S1.1. Atomic force microscopy

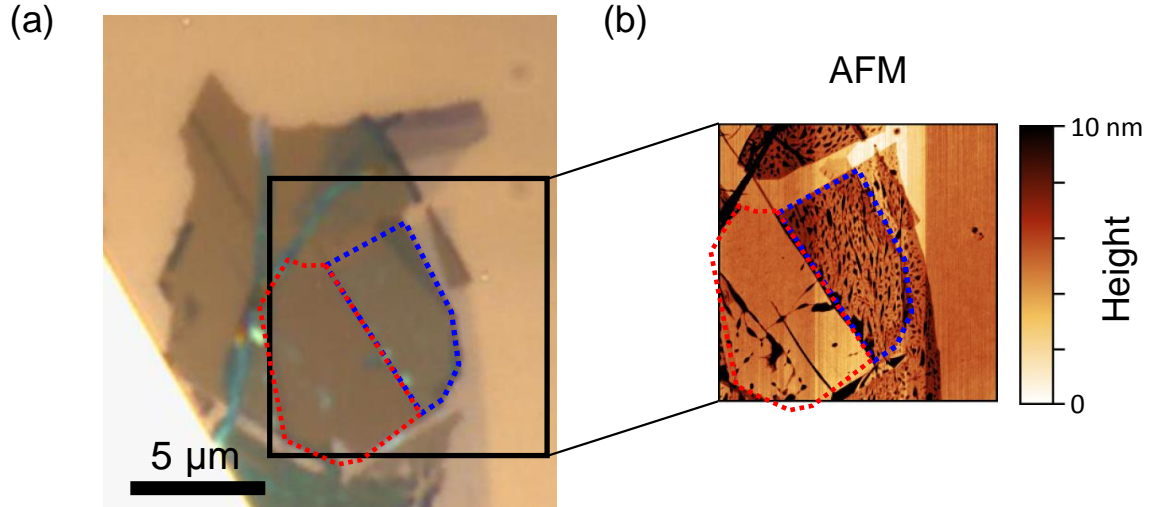


FIG. S1. (a) Optical image of the sample presented in the main text (denoted S1 in Fig. 4). (b) Atomic force microscopy image of the black square in (a). The coupled and decoupled regions are highlighted with red and blue dashed lines, respectively. In the coupled part, the interface between the two layers is free of contamination and is atomically flat due to the so-called “self-cleaning” mechanism [11, 91]. On the other hand, the interface in the decoupled part shows contamination pockets.

S1.2. Graphene Raman spectra for increasing Φ_{ph}

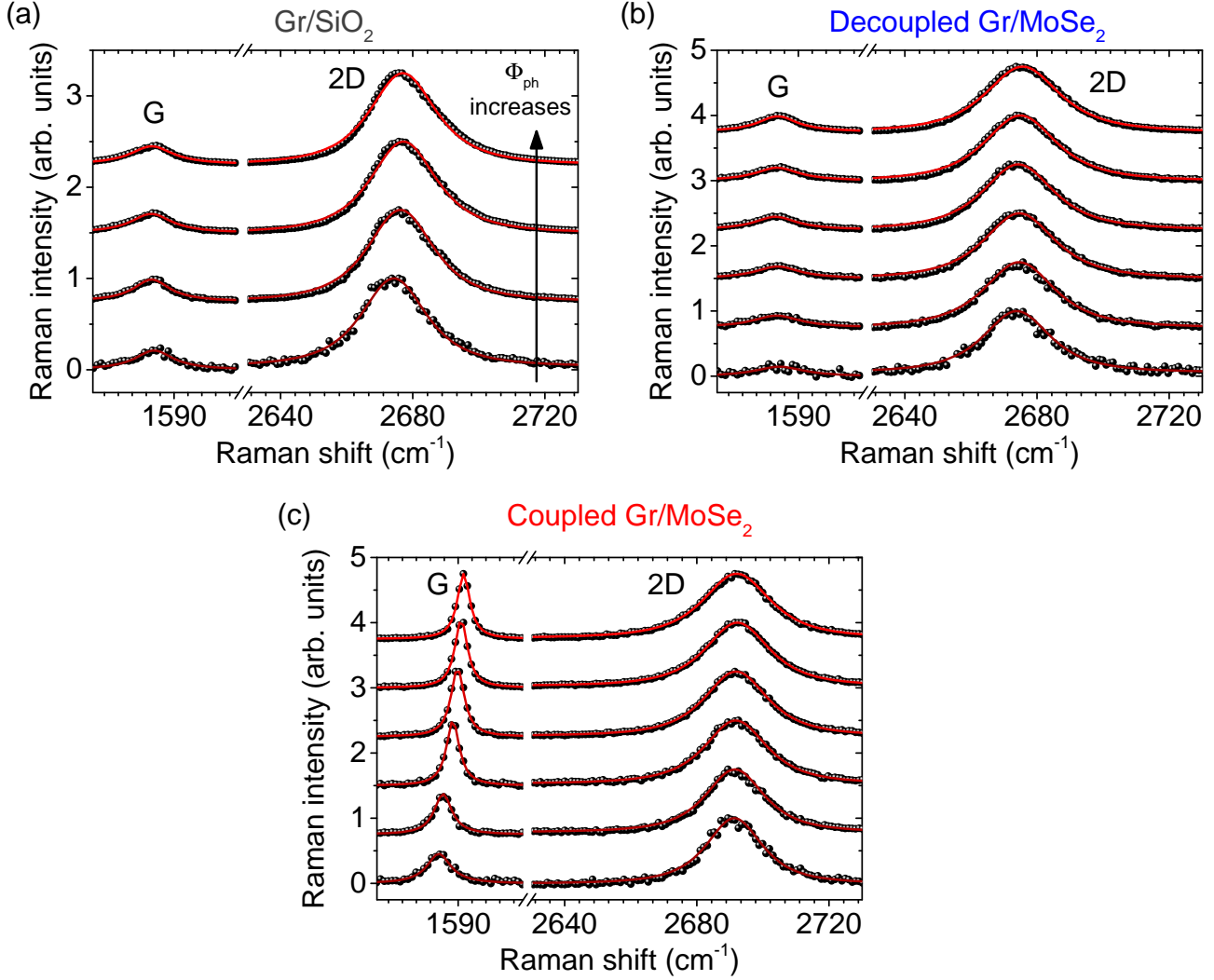


FIG. S2. Raman spectra corresponding to the data in Fig. 2. Measurements are performed in ambient conditions, at a photon energy $E_L = 2.33$ eV, for increasing values of incident photon flux (Φ_{ph}), between $3.3 \times 10^{20} \text{ cm}^{-2} \text{ s}^{-1}$ and $4.2 \times 10^{23} \text{ cm}^{-2} \text{ s}^{-1}$, for (a) Gr/SiO_2 , (b) decoupled and (c) coupled Gr/MoSe_2 . The spectra are vertically offset for clarity. Symbols are the experimental data and the solid lines are Lorentzian (G mode) and modified Lorentzian [92, 93] (2D mode) fits. A broad Lorentzian background has been subtracted from the G-mode spectra. We observe that the Raman spectra of Gr/SiO_2 and decoupled Gr/MoSe_2 are not affected by the increase of Φ_{ph} , whereas the Raman spectra of coupled Gr/MoSe_2 reveal clear fingerprints of photoinduced electron transfer (see main text).

S1.3. MoSe₂ Raman spectra for increasing Φ_{ph}

S1.3.1. A'_1 mode

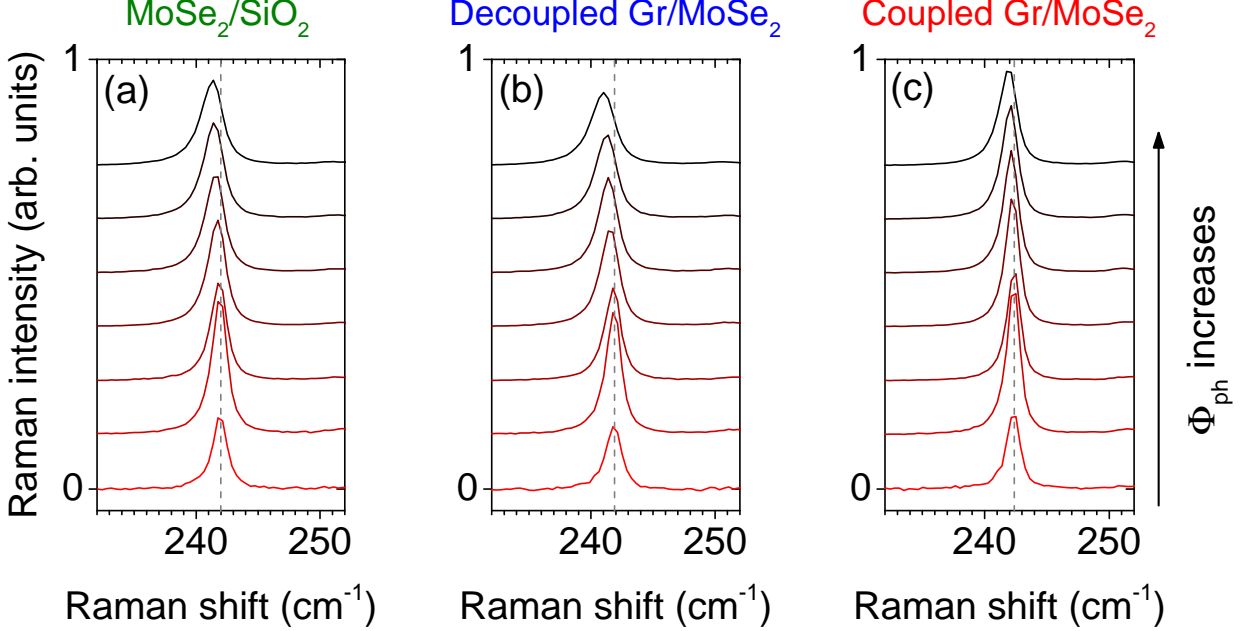


FIG. S3. Raman spectra of the A'_1 -mode feature in MoSe₂ recorded in ambient conditions at $E_{\text{L}} = 2.33$ eV for increasing values of incident photon flux (Φ_{ph}), between 3.3×10^{20} cm⁻² s⁻¹ and 6.7×10^{23} cm⁻² s⁻¹ for (a) Gr/SiO₂, (b) decoupled and (c) coupled Gr/MoSe₂. The spectra are vertically offset for clarity. The vertical gray dashed lines indicate the frequency measured at the lowest Φ_{ph} .

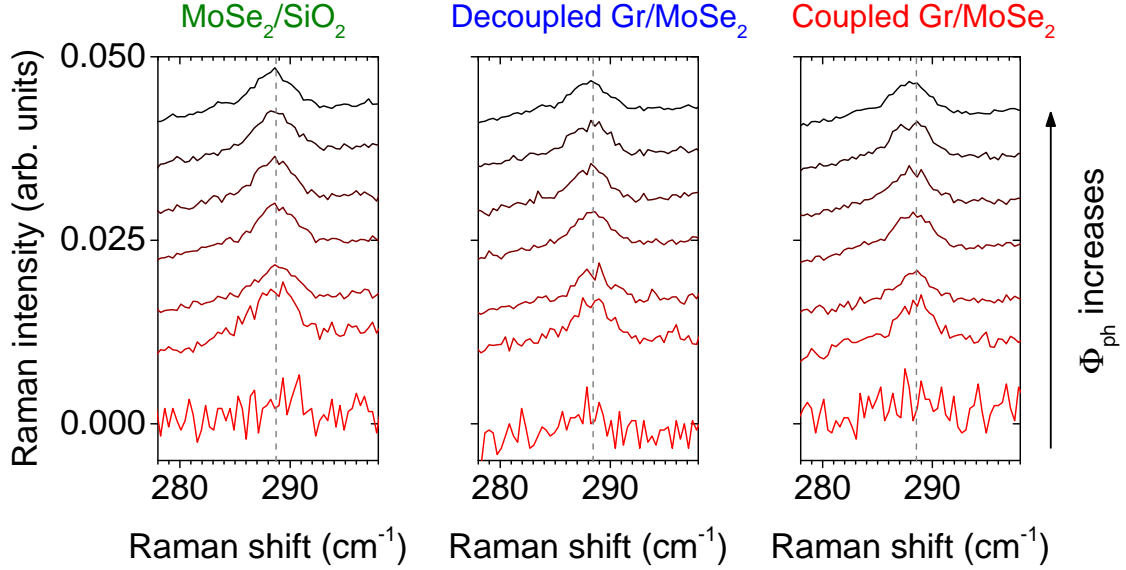
S1.3.2. E' mode

FIG. S4. Raman spectra of the E' -mode feature in MoSe_2 recorded in ambient conditions at $E_L = 2.33$ eV for increasing values of incident photon flux (Φ_{ph}), between $3.3 \times 10^{20} \text{ cm}^{-2} \text{ s}^{-1}$ and $6.7 \times 10^{23} \text{ cm}^{-2} \text{ s}^{-1}$ for (a) Gr/SiO_2 , (b) decoupled and (c) coupled Gr/MoSe_2 . The spectra are vertically offset for clarity. The vertical gray dashed lines indicate the frequency measured at the second lowest Φ_{ph} .

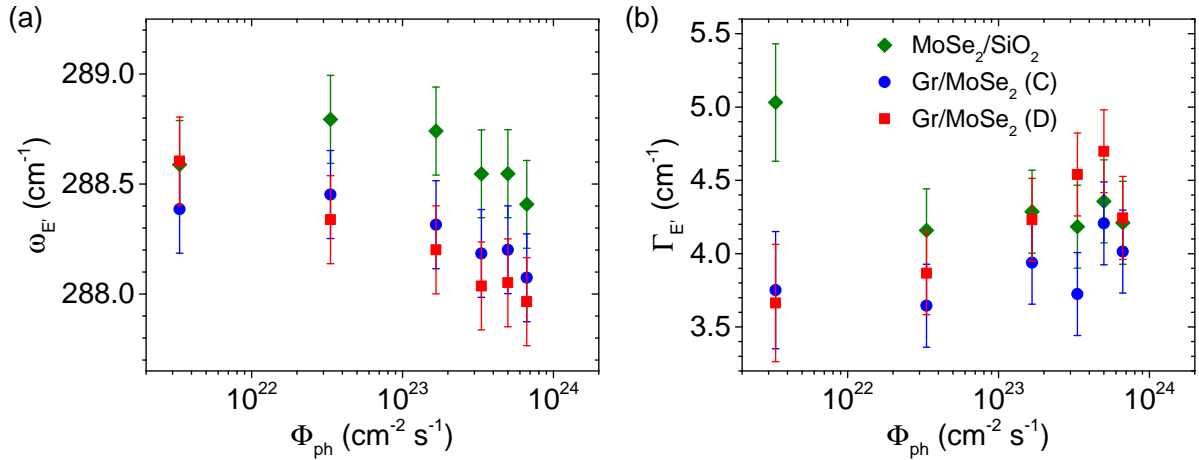


FIG. S5. Extracted (a) frequency $\omega_{E'}$ and (b) FWHM $\Gamma_{E'}$ from Fig. S8 as a function of the incident photon flux Φ_{ph} . Note that the spectra at $3.3 \times 10^{20} \text{ cm}^{-2} \text{ s}^{-1}$ were not fit due to a weak signal. No significant changes with Φ_{ph} are observed.

S1.4. Spatially-resolved Raman studies

S1.4.1. Two-dimensional maps

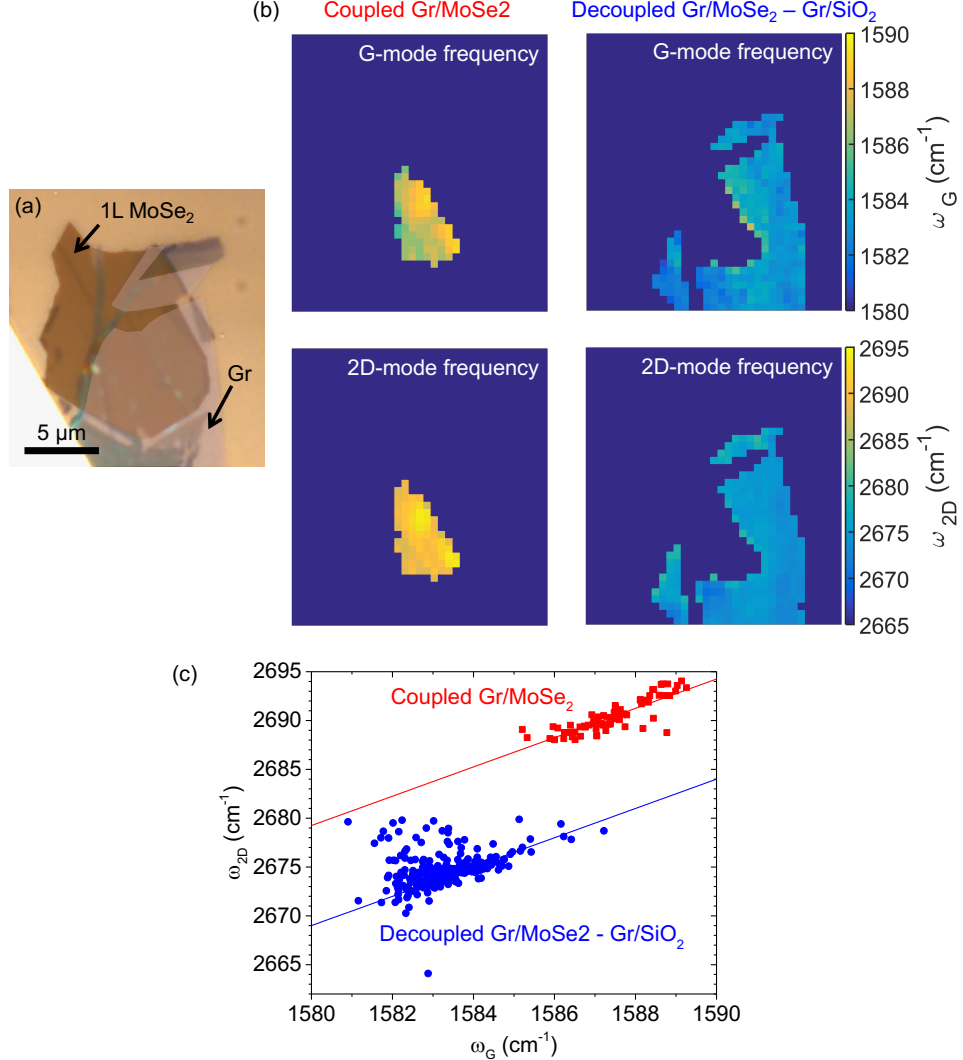


FIG. S6. (a) Optical image of sample 1. (b) G-mode frequency ω_G and 2D-mode frequency ω_{2D} for the coupled part of the heterostructure (left) or for the rest of the graphene monolayer (either deposited on SiO₂ or decoupled from MoSe₂, right). (c) Correlations between the frequencies of the 2D- and G-mode features shown in (b). The (ω_{2D}, ω_G) points cluster around mean values of $(2674.7 \pm 1.8 \text{ cm}^{-1}, 1583.3 \pm 0.9 \text{ cm}^{-1})$ on decoupled Gr/MoSe₂ and Gr/SiO₂ (blue circles), and $(2690.4 \pm 1.7 \text{ cm}^{-1}, 1587.4 \pm 0.9 \text{ cm}^{-1})$ on coupled Gr/MoSe₂ (red squares). Their dispersions around these mean values follow linear correlations with a same slope of ≈ 1.5 , that suggests the coexistence of both a native strain field (leading to a slope of ≈ 2.2) [55, 56] and unintentional doping heterogeneities (leading to a slope of $\approx 0.1 - 0.6$) [48, 55].

S1.4.2. Line scans at various incident photon fluxes

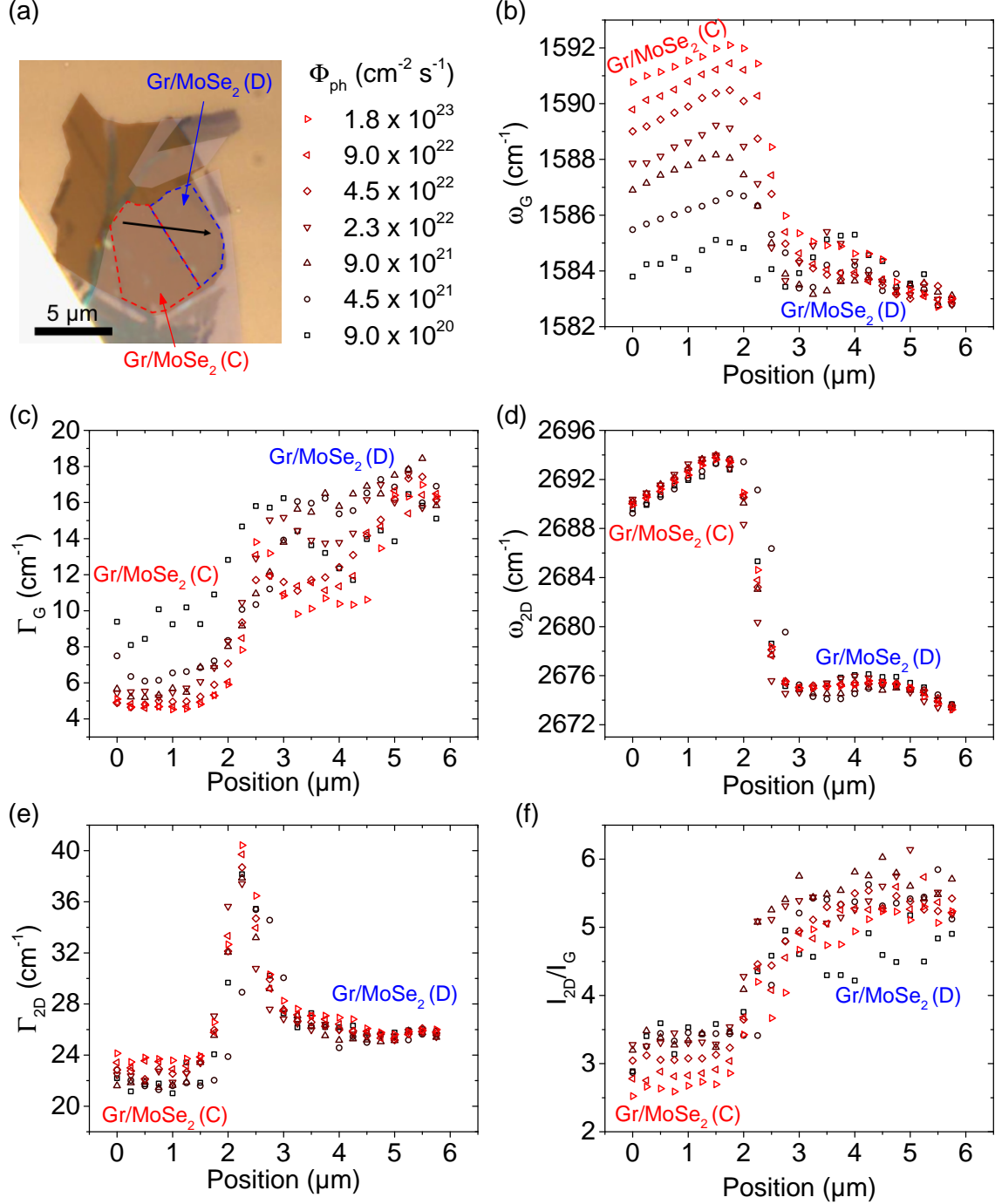


FIG. S7. (a) Optical image of sample S1. The red and blue dashed contours delimits the coupled and decoupled Gr/MoSe₂ regions. The line scans were recorded along the black arrow. The incident photon flux Φ_{ph} are indicated. (b) G-mode frequency ω_G , (c) G-mode FWHM Γ_G , (d) 2D-mode frequency $\omega_{2\text{D}}$, (e) 2D-mode FWHM $\Gamma_{2\text{D}}$ and (f) ratio between the integrated intensities of the 2D-and G-mode features $I_{2\text{D}}/I_G$ along the line scan.

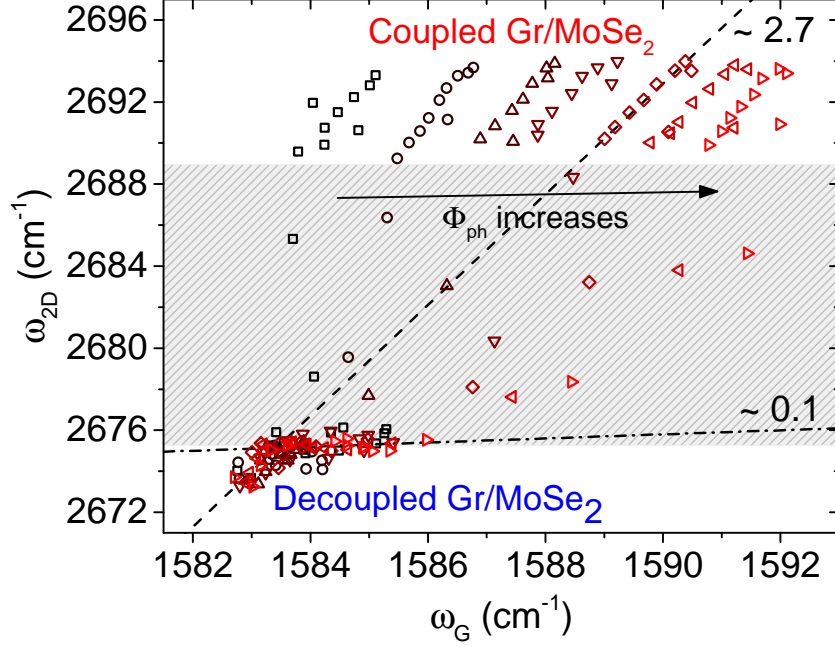


FIG. S8. Correlation between the 2D- and G-mode frequencies for the same line scans as in Fig. S3. The gray hatched area corresponds to the transition between decoupled and coupled Gr/MoSe₂. We notice that for decoupled Gr/MoSe₂, the (ω_{2D}, ω_G) points partly collapse onto a same line of slope ≈ 2.7 for all Φ_{ph} , while another set of points follows a linear correlation with a much reduced slope (≈ 0.1), typical from a slight electron doping [48]. In the coupled region, the (ω_{2D}, ω_G) points follow lines, again with a slope ≈ 2.7 that horizontally shift to higher ω_G for increasing Φ_{ph} . These observations are consistent with the conclusions drawn from the analysis of the Raman maps (see Figs. 1 and S3) and from the data in Fig. 2. This horizontal shift corresponds to the increase of doping with Φ_{ph} . The slope of ≈ 2.7 is in qualitative agreement with the typical slope of ≈ 2.2 measured for graphene under biaxial strain [56], and suggests negligible contributions from inhomogeneous doping in this restricted region (note that fingerprints of inhomogeneous doping are observed on the extended maps shown in Fig. S3).

S2. ADDITIONAL RESULTS OBTAINED ON OTHER SAMPLES

S2.1. Interlayer charge transfer in a Gr/MoSe₂ heterostructure with an initially hole-doped graphene layer

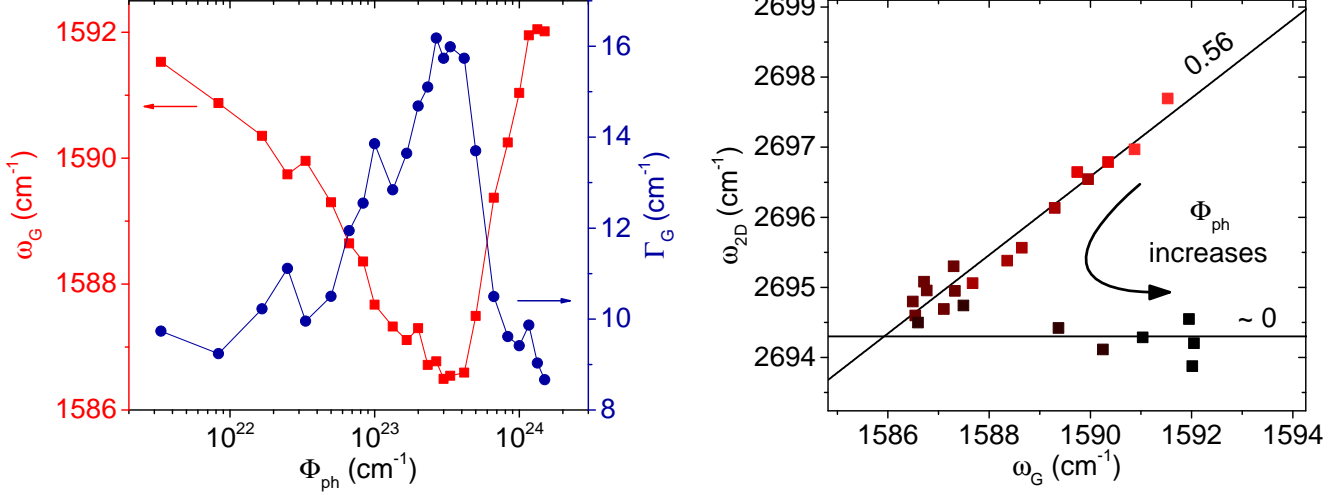


FIG. S9. (a) Frequency ω_G (red circles and lines, left axis) and FWHM Γ_G (blue circles and lines, right axis) of the G-mode feature measured on Sample S₃ (see Fig. 4a) at 2.33 eV under ambient conditions as a function of the incident photon flux Φ_{ph} . Lines are guides to the eye. (b) Correlations between the frequencies of 2D- and G-mode features under increasing photon flux Φ_{ph} . We observe a clear linear correlation along two lines with different slopes. At low Φ_{ph} , the frequencies follow a line of slope 0.56 corresponding to hole doping [48], while after crossing the charge neutrality point, the frequencies are aligned along a quasi-horizontal line corresponding to electron doping [48] (see also Fig. 2f). As a result, the graphene flake is initially hole-doped and photoexcited electrons are transferred from MoSe₂ to graphene.

S2.2. Laser-assisted desorption of molecular adsorbates under high vacuum

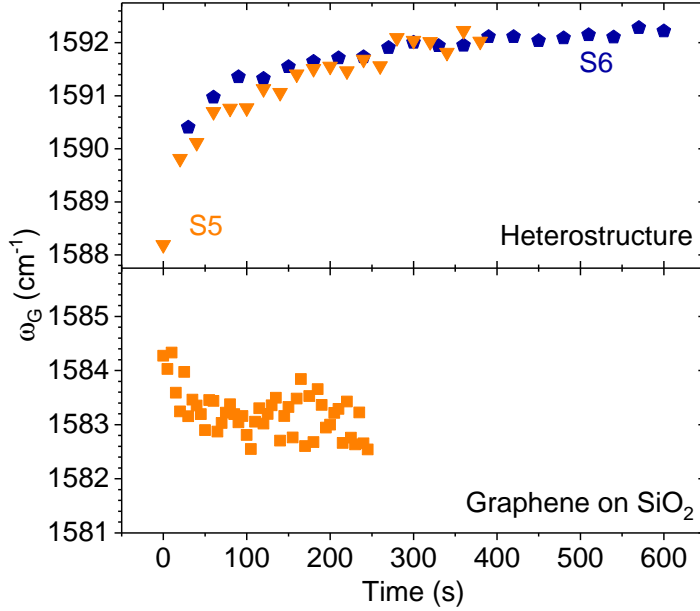


FIG. S10. Frequency of the Raman G mode (ω_G) measured as a function of time under high vacuum on $\text{MoSe}_2/\text{Gr}/\text{SiO}_2$ (sample S₅), $\text{Gr}/\text{MoSe}_2/\text{SiO}_2$ (sample S₆) (upper panel) and on a reference graphene monolayer sample on SiO_2 (lower panel). Measurements were performed at $\Phi_{\text{ph}} \sim 5 \times 10^{23} \text{ cm}^{-2} \text{ s}^{-1}$. The samples had not been illuminated before the measurements.

S2.3. Photoluminescence quenching on various samples

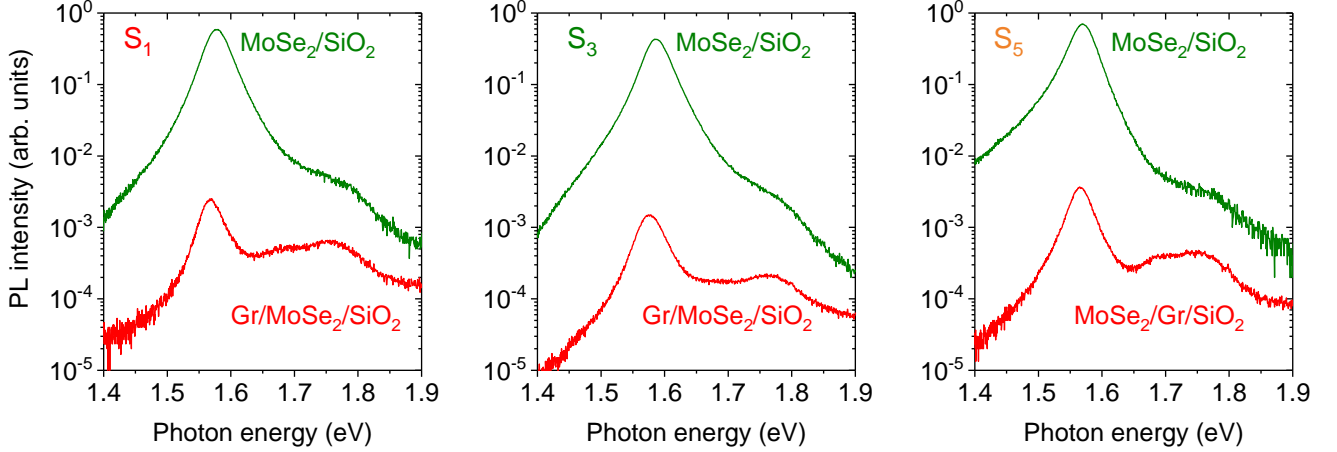


FIG. S11. Comparison between the photoluminescence spectra recorded on $\text{MoSe}_2/\text{SiO}_2$ and coupled Gr/MoSe_2 in ambient air at low $\Phi_{\text{ph}} < 10^{21} \text{ cm}^{-2} \text{ s}^{-1}$ on samples S_1 , S_3 , and S_5 . Very similar quenching factors and PL lineshapes are observed. Note that sample S_5 is an *inverted* $\text{MoSe}_2/\text{Gr}/\text{SiO}_2$ heterostructure.

S2.4. Exciton dynamics in ambient air and in vacuum

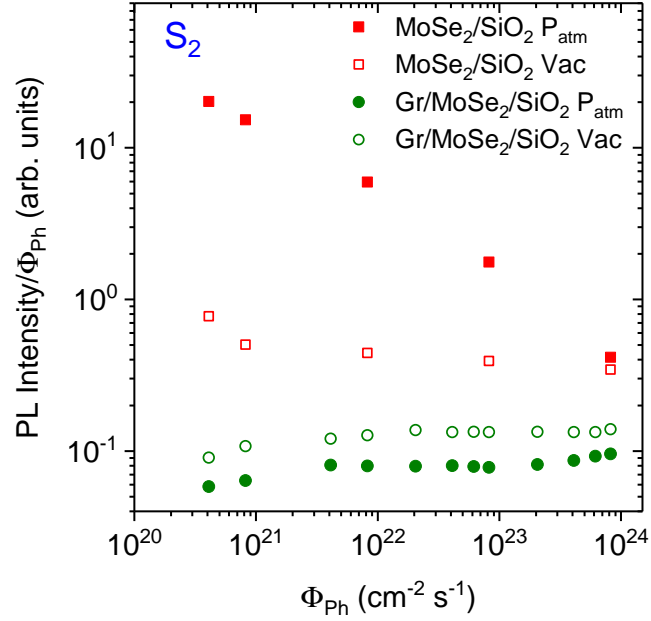


FIG. S12. Integrated photoluminescence intensity normalized by Φ_{ph} recorded on $\text{Gr}/\text{MoSe}_2/\text{SiO}_2$ (sample S_2) in ambient air (filled symbols) and in high vacuum (open symbols) as a function of Φ_{ph} .

S2.5. Comparison between photoinduced doping and exciton dynamics

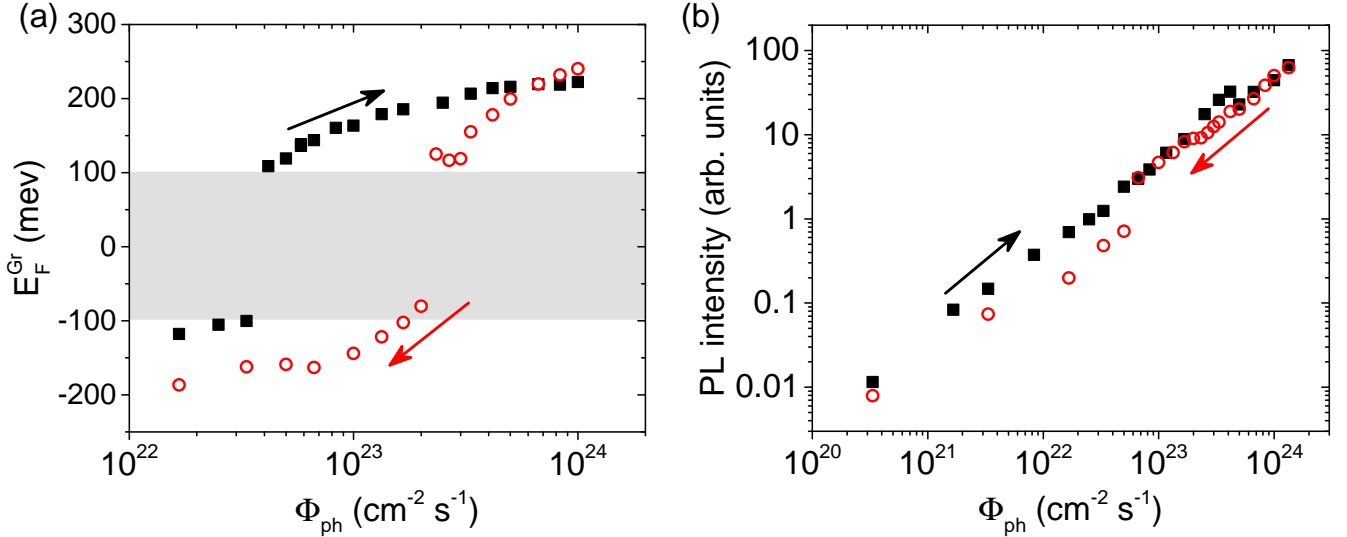


FIG. S13. (a) Fermi energy in graphene and (b) integrated intensity of the MoSe₂ A exciton photoluminescence as a function of the Φ_{ph} for a forward (black squares) and backward (open red circles) sweep of Φ_{ph} . The measurements were recorded on sample S₃.

Figure S13 shows PL and Raman measurements recorded in ambient air on Sample S₃ (see also Fig. S9) along a forward sweep followed by a backward sweep of Φ_{ph} . As opposed to most samples studied in this work, the graphene layer is *p*-doped at low Φ_{ph} and we clearly see that E_F^{Gr} (extracted following the procedure described in the text) has a hysteretic behavior that we attribute to laser-assisted adsorption of electron trapping molecules, such as water or molecular oxygen [94]. Remarkably, the (linear) evolution of the PL intensity is non-hysteretic, and thus largely independent on the equilibrium value of E_F^{Gr} obtained at a given Φ_{ph} . These results further confirm that the ICT processes are likely not solely responsible for the massive PL quenching in Gr/MoSe₂, and that molecular adsorbates to affect the charge transfer dynamics.

S2.6. Measurements under quasi-resonant optical excitation

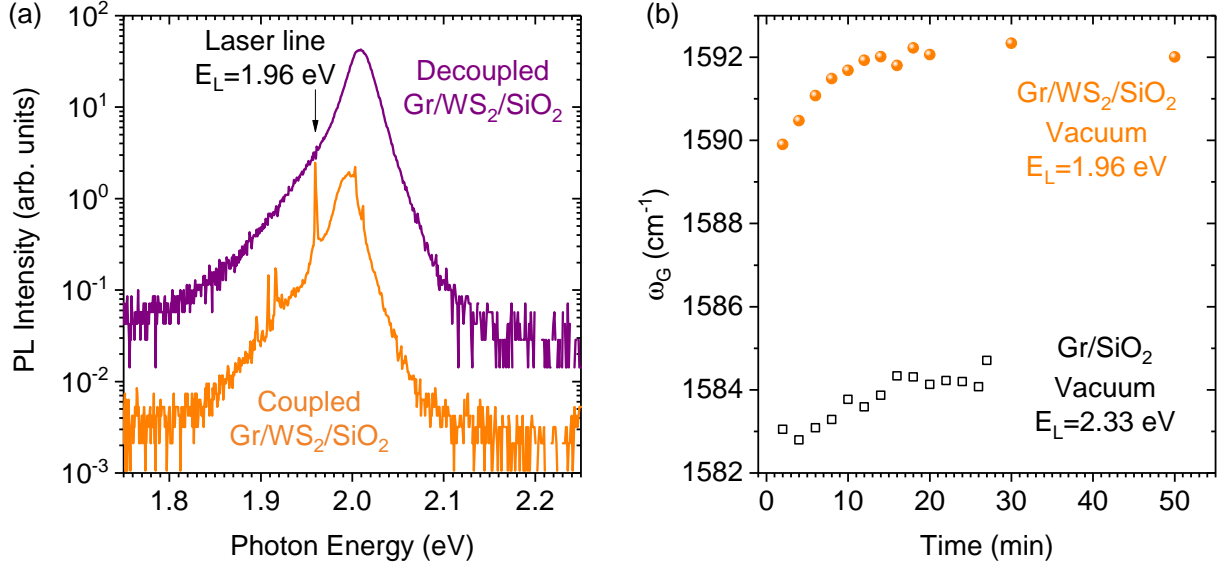


FIG. S14. PL and Raman measurements on a Gr/WS₂/SiO₂ heterostructure. The PL spectra in (a) are recorded at $\Phi_{\text{ph}} < 10^{20} \text{ cm}^{-2} \text{ s}^{-1}$ using a laser photon energy $E_L = 1.96 \text{ eV}$ slightly below the optical bandgap of WS₂ [54]. In these conditions, A excitons only can be formed by means of an upconversion process [84, 85]. Strong PL quenching is observed when comparing the PL intensity from coupled Gr/WS₂/SiO₂ (orange) to the PL intensity PL from a nearby decoupled Gr/WS₂/SiO₂ region (purple). The sharp lines above (below) the laser line in the coupled Gr/WS₂/SiO₂ spectra correspond to the anti-Stokes (Stokes) Raman modes of WS₂. (b) Evolution of the Raman G-mode frequency ω_G measured in vacuum as a function of time (similar to Fig. S10) on coupled Gr/WS₂/SiO₂ at $E_L = 1.96 \text{ eV}$ ($\Phi_{\text{ph}} \sim 5 \times 10^{23} \text{ cm}^{-2} \text{ s}^{-1}$). For comparison, a reference measurement performed on the same sample on a Gr/SiO₂ region is also shown. The upshifted ω_G relative to this reference is a clear fingerprint of photoinduced doping, as it has been thoroughly discussed on Gr/MoSe₂.

S3. DISCUSSION ON THE FREQUENCY OF THE 2D-MODE FEATURE

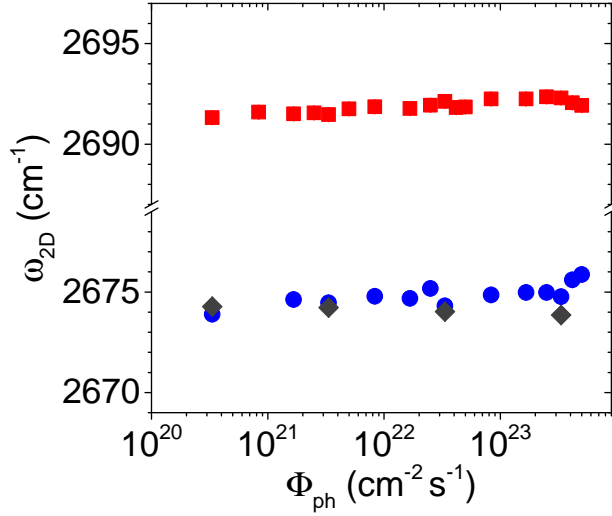


FIG. S15. 2D-mode frequency ω_{2D} measured in ambient air as a function of Φ_{ph} on sample S_1 .

In this section, we briefly comment on the rigid upshift of the 2D-mode frequency observed in coupled Gr-MoSe₂. Figs. 1(i) and 2(d) in the main text, and Figs. S2-S5 reveal a rigid upshift of $\approx 15 \text{ cm}^{-1}$ in coupled Gr/MoSe₂ as compared to Gr/SiO₂ and decoupled Gr/MoSe₂. This upshift cannot be explained by a change of doping [48]. The 2D mode shows more sensitivity to mechanical strain than to doping. However, an upshift of the 2D-mode frequency of around 15 cm^{-1} caused by strain would also lead to a G-mode upshift of around 7 cm^{-1} [55, 56], irrespective of Φ_{ph} . Such a shift is clearly not observed in all the figures cited above. Interestingly, a similar upshift of the 2D-mode feature has been observed in graphene deposited of thick boron nitride (BN) flakes [57, 58]. For Gr/BN, the 2D-mode upshift has been tentatively explained by dielectric screening due to the thick BN substrate, which reduces the electron-phonon coupling at the K and K' points. It is not obvious that a similar explanation could hold for Gr/single-layer TMD because of the atomic thickness of the TMD. Since the 2D-mode feature interweaves the electron and phonon dispersions [53, 92, 93, 95, 96], another possible explanation could be the modification of the graphene band structure due to van der Waals coupling to MoSe₂. However, in the case of MoS₂/SLG, it has been calculated that the effects of the interaction on graphene band structure at Γ , K and K' can be neglected [23, 97]. This intriguing observation of significant 2D-mode stiffening in vdWH will need further theoretical investigations to be fully understood.

S4. DISCUSSION ON OPTICAL INTERFERENCE EFFECTS

Optical interferences are known to affect the PL and Raman scattering response of 2DM deposited on layered substrates such as Si/SiO₂ [98–101]. Here, we calculated a PL enhancement of only 5 % for air/MoSe₂/SiO₂/Si as compared to air/Gr/MoSe₂/SiO₂/Si. This value is much too low to explain the observed PL quenching. We also calculated that for Gr/MoSe₂, optical interference effects lead to a negligible enhancement of I_{2D}/I_G by about 4 % as compared to the case of Gr/SiO₂.